Influence of ageing on the corrosion behaviour of 2024 aluminium alloy coated with a trivalent chromium conversion layer

R. Saillard, S. Zanna, A. Seyeux, B. Fori, Jolanta Światowska, C. Blanc, P. Marcus

Influence of ageing on the corrosion behaviour of 2024 aluminium alloy coated with a trivalent chromium conversion layer

R. Saillard [a], S. Zanna [b], A. Seyeux [b], B. Fori [c], J. Światowska [b], C. Blanc [a,*], P. Marcus [b]

[a] CIRIMAT, Université de Toulouse, CNRS, INP-ENSIACET, 4 allée Emile Monso, BP 44362, 31030, Toulouse cedex 4, France
[b] PSL Research University, Chimie ParisTech-CNRS, Institut de Recherche de Chimie Paris (IRCP), 75005, Paris, France
[c] MECAPROTEC Industries, 34 Boulevard de Joffrery, BP 30204, 31605, Muret Cedex, France

ARTICLEINFO

Keywords:
A. Aluminium
A. Copper
B. ToF-SIMS
B. XPS
B. EIS
C. Oxide coatings

ABSTRACT

Time-of-flight secondary ion mass spectrometry and X-ray photoelectron spectroscopy were used to study the influence of ageing of 2024 aluminium alloy at 190 °C on subsequent degreasing and deoxidation behaviour. After degreasing and deoxidation of the aged alloy, an increase in the surface Cu coverage and a surface roughening were observed as compared to a non-aged alloy. The Cu surface enrichment affected the growth mechanisms of the trivalent chromium process (TCP) coating. The TCP coating formed on an aged sample was thicker, but more defective leading to the decrease of its anticorrosion properties, as compared to a non-aged sample.

1. Introduction

In order to reduce the emission of polluting gases in the aeronautics sector, Al alloys are of great interest for aircraft structures, due to their low density, close to 2.7 g cm^{-3} [1], and because their mechanical properties (yield strength and ultimate tensile strength) are significantly better in comparison to pure Al due to addition of alloying elements such as Cu, Mg or Li [2,3]. For aircraft manufacturing, the 2024 Al alloy (AA2024), with Cu and Mg as the major alloying elements, is one of the most used alloys. It has a heterogeneous microstructure, with, in particular, the presence of intermetallic coarse particles (IMCs) with different chemical compositions [4–7]. When AA2024 is exposed to an aggressive electrolyte, localised corrosion, in particular pitting corrosion, occurs [8–14] due to the difference in electrochemical potential between IMCs and the alloy matrix. Thus, to protect the AA2024 against corrosion, surface treatments are required for industrial applications.

In the aircraft industry, when electrical conductivity of the alloy is required, thin conversion layers are applied and the most commonly used are the hexavalent Cr-based conversion treatments due to their very good anticorrosion and self-healing properties [15–19]. However, hexavalent Cr has been classified as a CMR (carcinogenic, mutagenic or toxic for reproduction) agent by the European REACH regulation (Restriction, Evaluation and Authorisation of CHemicals) [18,20]. Therefore, a new promising conversion treatment process based on trivalent Cr, known as trivalent Cr process (TCP), has been developed in the aeronautic sector [21]. As described in the literature, this treatment leads to formation of a duplex structure composed of a fluoroaluminate-rich inner part and a Cr and Zr oxide- and hydroxide-rich outer part [22–24]. The formation mechanism of the TCP coating is based on the reduction of protons, that leads to a pH increase near the surface and then to the precipitation of Cr and Zr as oxides and hydroxides [24–27]. Depending on the underlying alloy chemistry and microstructure, the oxidation-reduction reactions can be modified, and therefore the growth kinetics of the TCP coating can be affected. For AA2024, Cu-rich IMCs can have a significant influence on the TCP coating growth. As demonstrated by Qi et al., the reduction of protons that occurs preferentially on cathodic IMCs leads to the formation of a thicker conversion layer on those particles [28]. The same phenomenon was observed on AA7075 by Munson et al. [29]. It was shown that the increase in the growth kinetics of the TCP coating on Cu-rich IMCs led to the formation of a locally thicker conversion layer, but more defective, and therefore with poor anticorrosion properties [28,30]. Moreover, by studying several 7xxx Al alloys, Meng et al. showed that the detrimental effect of Cu on the growth of thicker and more defective conversion layer was due to the surface enrichment in Cu during the pre-treatment steps [31]. However, in Cu-containing Al alloys, such as AA2024, Cu can be present in IMCs, but also in the supersaturated solid solution or in the hardening precipitates depending on the metallurgical state of the alloy,

* Corresponding author.
E-mail address: christine.blanc@ensiacet.fr (C. Blanc).

so that the surface Cu coverage measured after the pre-treatment steps cannot be only related to the dissolution of Cu-rich IMCs.

The aim of this study was to evaluate the influence of ageing on the corrosion behaviour of TCP coated AA2024. Considering that ageing was mainly associated with changes in Cu distribution in the alloy resulting from precipitation phenomena, attention was paid to the influence of Cu on the growth of the TCP coating formed on AA2024 as a function of the Cu state in the alloy, i.e. Cu in solid solution or as part of a precipitate (IMC, intragranular and/or intergranular precipitates). Therefore, two samples of AA2024 were compared: a naturally aged sample and an artificially aged at 190 °C sample in order to modify the Cu distribution in the alloy. The chemical composition of the oxide layer formed on the sample surface before and after the degreasing and deoxidation steps was studied. The TCP coating was then formed and analysed by X-ray Photoelectron Spectroscopy (XPS) and Time-of-Flight Secondary Ion Mass Spectrometry (ToF-SIMS) for both naturally and artificially aged samples. Finally, electrochemical characterisations were performed for the coated samples using potentiodynamic polarisation tests and electrochemical impedance spectroscopy measurements to study the relationship between the chemical composition and structure of the TCP coating and its anticorrosion properties.

2. Materials and methods

2.1. Materials and preparation of the TCP coated samples

The 3 mm-thick AA2024 sheet contained 4.4 % Cu, 1.4 % Mg, 0.15 % Fe, 0.51 % Mn (in wt. %). The as received alloy was in the T3 metallurgical state (hot and cold rolled, solution heat treated at 495 °C and then water quenched, stress relieved and naturally aged at room temperature for 4 days). These samples are referred to as Reference samples. Some T3-samples were artificially aged at 190 °C for 12 h in air followed by a cooling at room temperature; these samples are referred to as 190–12 samples. Before the degreasing and deoxidation, and before the ageing treatment, the Reference and the 190–12 samples, respectively, were mechanically ground with abrasive paper from SiC 1200 to SiC 4000 and then polished with diamond paste down to 1 µm. After polishing, the samples were ultrasonically cleaned in demineralised water during 30 s.

Before the TCP coating deposition, the samples were submitted to degreasing and deoxidation. They were first rinsed with acetone. The degreasing consisted in a 20-minute immersion at 60 °C in a pH 9 alkaline solution (40 g L^{-1} of sodium tripolyphosphate, 40 g L^{-1} of borax and 5 mL L^{-1} of Turco 4215 additive). For deoxidation, the samples were immersed for 5 min at 50 °C in a pH=1 sulfo-nitro-ferric Socosurf A1858/A1806 solution (provided by Socomore, France). After the degreasing and deoxidation, samples were immersed for 10 min without stirring at 40 °C in a pH=3.9 TCS conversion solution (32 % v/v Socosurf TCS provided by Socomore, France) to form the TCP coating. Then, they were immersed for 5 min at room temperature in the post-treatment bath (10 % v/v Socosurf PACS provided by Socomore, France, 5% v/v H_20_2 at 35 % v/v in water, pH between 4.2 and 5.3). Before each step, the samples were rinsed in deionised water. They were dried during 10 min at 60 °C and stored in the laboratory air for 48 h before any experiment.

2.2. Experimental methods and techniques

2.2.1. Analysis of the microstructure

The surface area fraction covered by the IMCs particles on polished surfaces, and the average grain size after electrochemical etching (Flick reagent: 3.5 mL HBF_4 for 96.5 mL deionised water) were determined by using an optical microscope (OM, *Nikon MA200*). Smaller and thinner precipitates were observed using a Transmission Electron Microscope (TEM) operated at 200 kV (*JEOL JEM 2100 F*) in the Raimond Castaing Microanalysis Center in Toulouse. For TEM samples, transparency to electrons was obtained by mechanical grounding with SiC abrasive paper (1200, 2400 and 4000) to reach a thickness of 100 µm. Then, the samples were cut in 3 mm diameter discs, and then electropolished in *TenuPol-5* (900 mL CH_3OH and 300 mL HNO_3) at –15 °C. A microhardness instrument (*BUEHLER Omnimet-2100*), equipped with a 500 g load Vickers indenter, was also used to determine the hardness of the samples, and consequently to characterize the precipitation hardening state.

2.2.2. Chemical and morphological characterisation of the sample surface

The surface chemical composition was analysed using an XPS spectrometer (*Thermo Electron ESCALAB 250*) operating at a base pressure of 10^{-9} mbar in the analysis chamber. For all analyses, an Al Kα (hυ = 1486.6 eV) monochromatised X-ray source was used with a take-off angle of 90°. The spectrometer was calibrated using clean Cu (932.6 eV), Ag (368.2 eV) and Au (84.1 eV). The survey spectra were recorded with a 100 eV pass energy, whereas high resolution core level spectra of C 1s, Al 2s, Mg 2p and Cu 2p were recorded with a 20 eV pass energy. Due to the close binding energies of Al 2p and Cu 3p peaks, the Al 2s spectrum was measured instead of Al 2p. The Advantage software version 5.938 (*Thermo Electron*) was used for data processing. The peak fitting was performed using a Shirley-type background.

A ToF-SIMS V spectrometer (*ION TOF GmbH*) was used to characterise the surface and in-depth composition of oxide layers and TCP coatings. For the analyses, the main chamber pressure was maintained at approximately 10^{-9} mbar. ToF-SIMS in-depth profiles were recorded using a pulsed 25 keV Bi^+ primary ion source delivering a 1.2 pA of target current over a 100 × 100 µm² area, interlaced with a 2 keV Cs^+ sputter beam delivering 100 nA of current over a 400 × 400 µm² area. Both ion beams were at a 45° incidence to the specimen surface and aligned in such a way that the analysed area was in the centre of the sputtered crater. Negative ion depth profiles were recorded because of their higher sensitivity to fragments coming from oxide matrices. The data were post-processed using the Ion-Spec software 6.5 version.

The surface roughness of the samples after degreasing and deoxidation was determined using a PicoPlus 5500 Agilent atomic force microscope (AFM) in the tapping mode. The probe was a conductive Pt-coated silicon tip. The data were then processed using the analysis software Picoview 1.8.

Field emission gun SEM observations (FEG-SEM) using a JEOL JSM 7800 F Prime in the Raimond Castaing Microanalysis Center in Toulouse were also performed to characterise the surface morphology after degreasing and deoxidation, as well as the TCP coating (cross-section). Observations were performed with secondary electrons (5 kV). For the FEG-SEM images (see results section), the horizontal scale given cannot be used for the vertical direction due to a tilt of the sample during imaging (a cos (38°) factor has to be applied).

2.2.3. Electrochemical measurements

Electrochemical measurements were performed with a potentiostat (*Biologic VSP-128*), in electrochemical cells (*Gamry Instruments PTC1™ Paint Test Cell*), by using a three-electrode set-up, with a 10 cm^2 surface area for the working electrode, a platinum electrode as a counter electrode and a saturated calomel reference electrode. Potentiodynamic polarisation curves (sweep rate of 0.07 mV s^{-1}) were plotted for the coated samples in a 0.5 M NaCl solution. The anodic and cathodic parts were recorded separately from the open circuit potential (OCP) after a 90-minute immersion at OCP. Electrochemical impedance spectroscopy measurements were also performed at OCP, for different immersion durations up to 30 days, to characterise the corrosion resistance of the coated samples. The frequency range was from 10^5 Hz to 10^{-2} Hz, and the potential modulation amplitude was 20 mV (rms). The surface Cu coverage of the sample was determined after degreasing first, and then after degreasing and deoxidation, by cyclic voltammetry (CV) in a deaerated solution (purged with N_2) of borate buffer solution with pH 8.4 (8.17 g L^{-1} of sodium borate ($Na_2B_4O_7$) and 7.07 g L^{-1} of boric acid

(H_3BO_3)). The CV experiment consisted in three CV scans from -0.70 V/SCE to 0.3 V/SCE then back to -1.2 V/SCE at a sweep rate of 1 mV s^{-1}. Samples were held at -0.70 V/SCE for 5 min, 10 min and 20 min before the first cycle, the second and the third, respectively. Only the third cycle was used to calculate the surface Cu coverage, the first two cycles allowing the signal corresponding to Al oxidation to be reduced. Therefore, the area under the Cu(0) → Cu(I) peak in the last scan was used to determine the relative electroactive Cu content. This method was described in details by Scully [32,33] and Davenport [34].

3. Results and discussion

3.1. Microstructure and surface characterisation of the uncoated samples

3.1.1. Microstructure of the Reference and 190 ~~1~~2 samples

Optical microscopy (OM) observations of both Reference and 190—12 samples showed a recrystallised microstructure (Fig. 1a), with a similar average grain size (22 µm in the rolling direction (RD) and 19.2 µm in the transverse direction (TD)), in accordance with the values reported in the literature [35,36]. Such a result was expected because the recrystallisation phenomenon occurred during the solution heat treatment, following the hot and cold rolling steps [37]. No deformation step of the sheet was added between the solution heat treatment and the ageing at 190 °C, so that no further modifications of the grain size were expected during the ageing.

The distribution and size of intermetallic coarse particles (IMCs) were similar also for the Reference and 190–12 samples (Fig. 1b). The formation of IMCs was due to the presence of impurities and excess alloying elements. During solidification, the concentration of some alloying elements (e.g. Cu, Mg, Fe and Mn) exceeded the solubility limit in the Al solid solution, especially in the liquid interdendritic zones, leading to the precipitation of IMCs. Their composition was widely discussed in the literature [7,9,12,38,39]. Two groups of IMCs were distinguished, the first corresponding to the Al-Cu-Mn-Fe type with an irregular shape, and the second to S-Al_2CuMg phase with a spherical shape. IMCs remained insoluble, so that the ageing treatment at 190 °C did not change their size and distribution. Therefore, for both samples, the mean surface area covered by one Al-Cu-Mn-Fe type particle was close to 7.3 μm^2 and that for the S-Al_2CuMg phase was close to 2.4 μm^2.

Observations at the TEM scale showed significant differences in microstructure between these two samples. Fig. 1c and d showed TEM micrographs for the Reference and 190–12 samples, respectively. Firstly, observations revealed particles identified as T-phase insoluble dispersoids [40,41] for both samples (shown by a red arrow in Fig. 1d). These particles were useful in controlling the recrystallisation phenomenon by blocking the movement of grain boundaries. Concerning the hardening precipitates, two precipitation sequences have been widely studied in the literature for AA2024, leading to the nucleation and growth of precursors of the θ-Al_2Cu phase or S-Al_2CuMg phase [42–44]. For the studied alloy, the Cu:Mg ratio was close to 3:1 and led

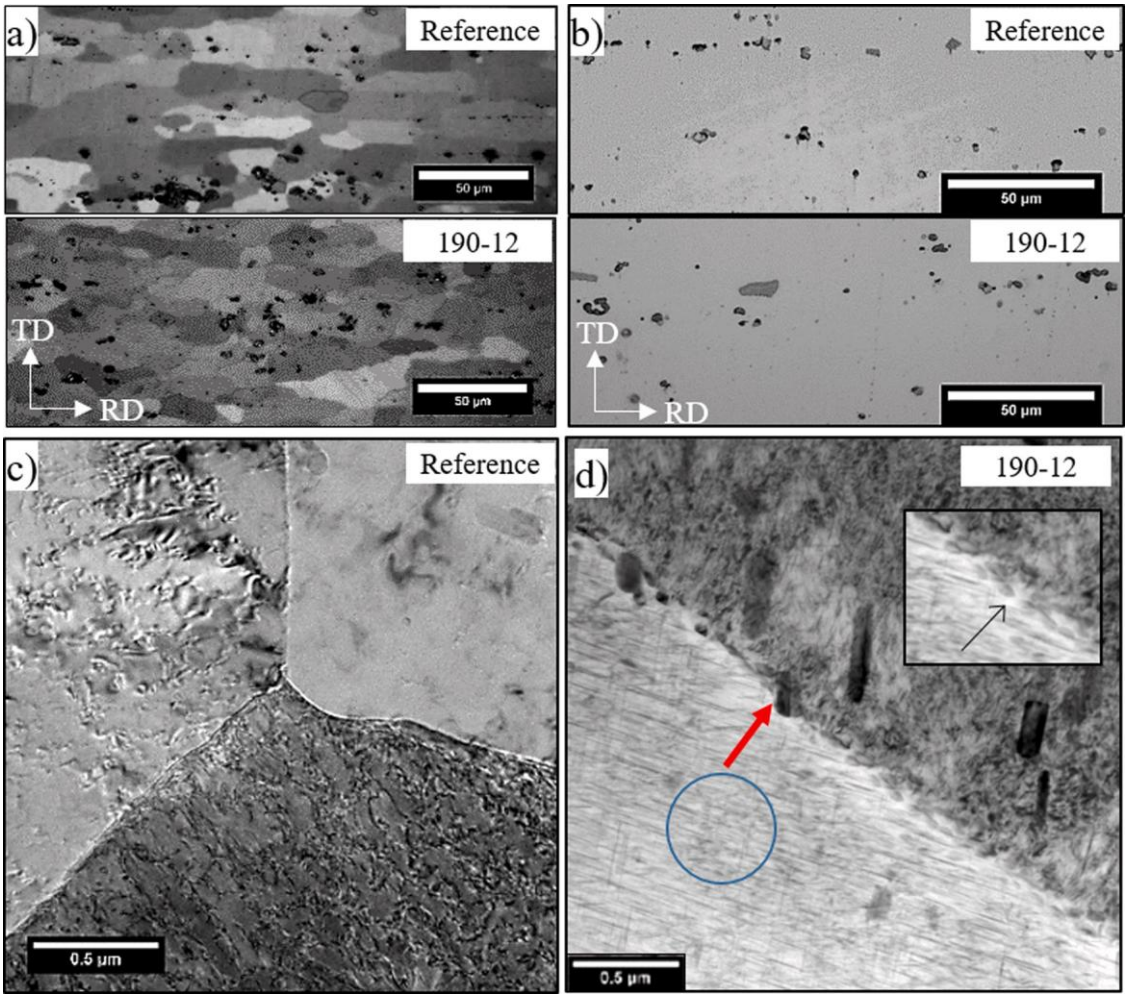

Fig. 1. OM images of the Reference and 190-12 samples a) the grain size after electrochemical etching with a Flick reagent and b) the distribution of the IMCs. TEM images of the c) Reference and d) 190-12 samples. The red arrow in Fig. d shows particles identified as T-phase insoluble dispersoids. The blue circle in Fig. d shows some hardening intragranular precipitates. The insert in Fig. d shows the fine precipitate-free zone (black arrow).

to the preferential nucleation of S-Al_2CuMg phase, as described by Bagaryatsky [44]:

SSS → GPB zone → S''/GPB2 → S′ → S-Al_2CuMg

where SSS was the supersaturated solid solution and GPB the Guinier-Preston-Bagaryatsky zones, i.e. Cu and Mg atoms ordered in a short range. The orthorhombic S'' or GPB2, with a $Al_5Cu_3Mg_3$ stoichiometry, was coherent with the matrix [45,46]. The composition of S′ and S phases was similar; nevertheless, the two phases had a slight difference in terms of orthorhombic lattice parameters [45,47,48]. For the Reference sample, high resolution TEM images (not shown here) did not reveal the presence of hardening intragranular precipitates. However, the presence of GPB zones was expected due to the previous thermo-mechanical treatment of the sheet, and the natural ageing at room temperature. The hardness values for the Reference sample close to 143 HV confirmed this assumption. The hardness of a freshly solution heat-treated sample was close to 90 HV [49–51]. For the 190−12 sample, continuous intergranular and dense hardening intragranular precipitates were observed (Fig. 1d, blue circle). As shown in a previous study [52], those precipitates were S/S′-Al_2CuMg phase with a base-centred orthorhombic network and belonging to the Cmcm space group in accordance with the literature data [41,48,53,54]. Finally, and in contrast to the Reference sample, a fine precipitate-free zone (PFZ) was observed for the 190—12 sample (insert in Fig. 1d).

3.1.2. Surface chemical characterisation of the Reference and 190 12– samples

First of all, the chemical composition of the sample surface before (Reference) and after thermal treatment (190–12) was analysed by ToF-SIMS and XPS (Figs. 2 and 3, respectively). Fig. 2 shows the characteristic ToF-SIMS negative ion depth profiles obtained for Reference and 190—12 samples to determine the composition and structure of the oxide films. Cu^- and Al_2^- ion signals represent the metallic Cu and Al, respectively, and CuO^-, AlO_2^- and MgO^- represent the oxidised (oxide and/or hydroxide) Cu, Al and Mg, respectively. These ions have been used previously to characterise Al-Cu alloy surfaces [23,55–57]. The intensity changes of different ions are shown, in a logarithmic scale to enhance the low intensity signals, as a function of sputtering time in s (bottom axis) and depth from the surface in nm (top axis). The sputtered depth was evaluated from the measurement of the crater depth at the end of the ToF-SIMS profile (down to the metallic substrate) by using a Veeco Dektak 150 contact profilometer. The measurement was performed only on the Reference sample according to the procedure described by Ely et al. [23]. It should be noted that this calibration done only for Reference sample could introduce an error in the sputtered depth evaluation for the 190–12 sample due to some differences in surface chemical composition between these two samples. The error was assumed to be negligible considering that the oxides formed on both samples were similar (see below).

Three main regions can be identified for both samples as a function of the intensity changes of metal (Cu^-, Al_2^-) and oxide-related (CuO^-, AlO_2^- and MgO^-) signals: oxide, intermediate region and the bulk sample region. These regions are indicated in Fig. 2 by vertical dashed lines.

For the Reference sample (Fig. 2a), the first region that extends to around 5 s of sputtering is characterised by an intense AlO_2^- signal, and low intensity of Al_2^- and Cu^-, which are signals characteristic of the metallic substrate. This region corresponds to an outer Al oxide layer that covers the metallic alloy substrate. In this region, the CuO^- and MgO^- signals remain very weak suggesting that the surface oxide is mainly composed of Al oxide. Al_2^- signal reaches a maximum intensity after 25 s of sputtering, corresponding to the bulk region. Here, at 25 s of sputtering time also a high intensity of Cu^- signal can be observed indicating that the metallic substrate is enriched in Cu as already reported in the literature [57]. The CuO^- signal, characteristic of the Cu oxide, follows the behaviour of the Cu^- signal and reaches its maximum intensity at the metal/oxide interface. This has been already observed by Cornette et al. [57] and is assigned to the partial oxidation of the IMCs at their surfaces. The region ranging between 5 s and 25 s of sputtering characterized by a progressive decrease of the AlO_2^- and increase of the Al_2^- signals, corresponds to an intermediate region. The presence of this intermediate region results from the roughness of the alloy substrate. Taking into account the oxide region and the intermediate region, mixing the inner oxide region and the metallic substrate, a minimum and a maximum oxide thickness can be calculated from the ToF-SIMS ion depth profile. Thus, a minimum oxide thickness corresponding to the first dashed line is around 2 nm and the maximum is around 9 nm. As the sputtering and analysis direction are at 45° to the surface, the shadowing effect resulting from the surface roughness leads to a slight

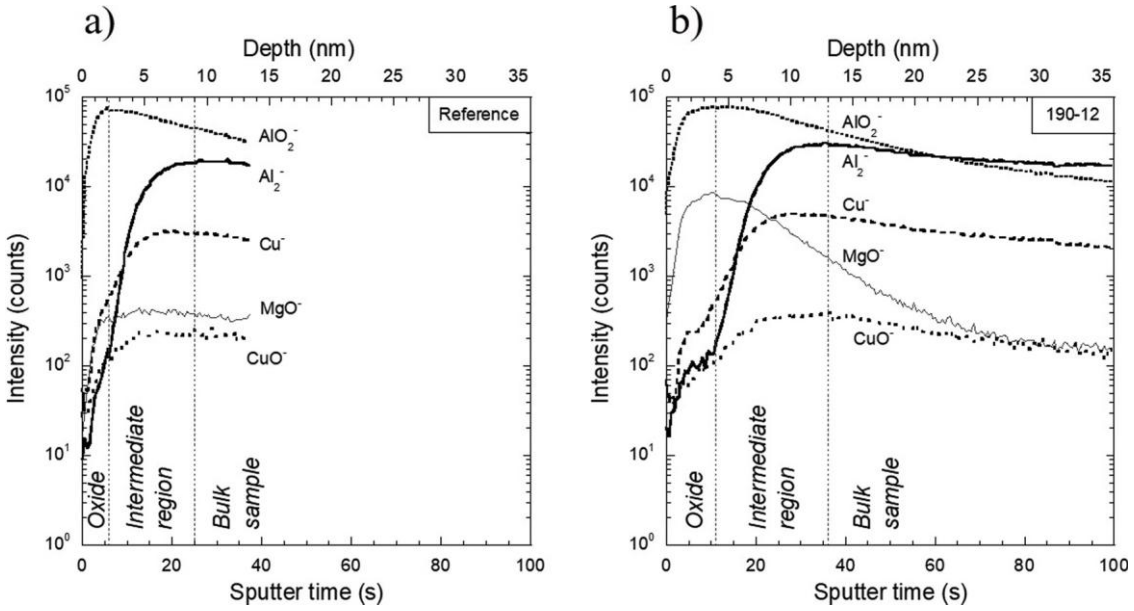

Fig. 2. ToF-SIMS negative secondary ion depth profiles: AlO_2^-, Al_2^-, Cu^-, CuO^-, MgO^- obtained for a) the reference AA2024-T3 sample (Reference) and b) the AA2024-T3 sample after thermal treatment at 190 °C during 12 h (190-12). Dashed vertical lines indicate 3 regions: oxide, intermediate region between the oxide and bulk sample and bulk sample region.

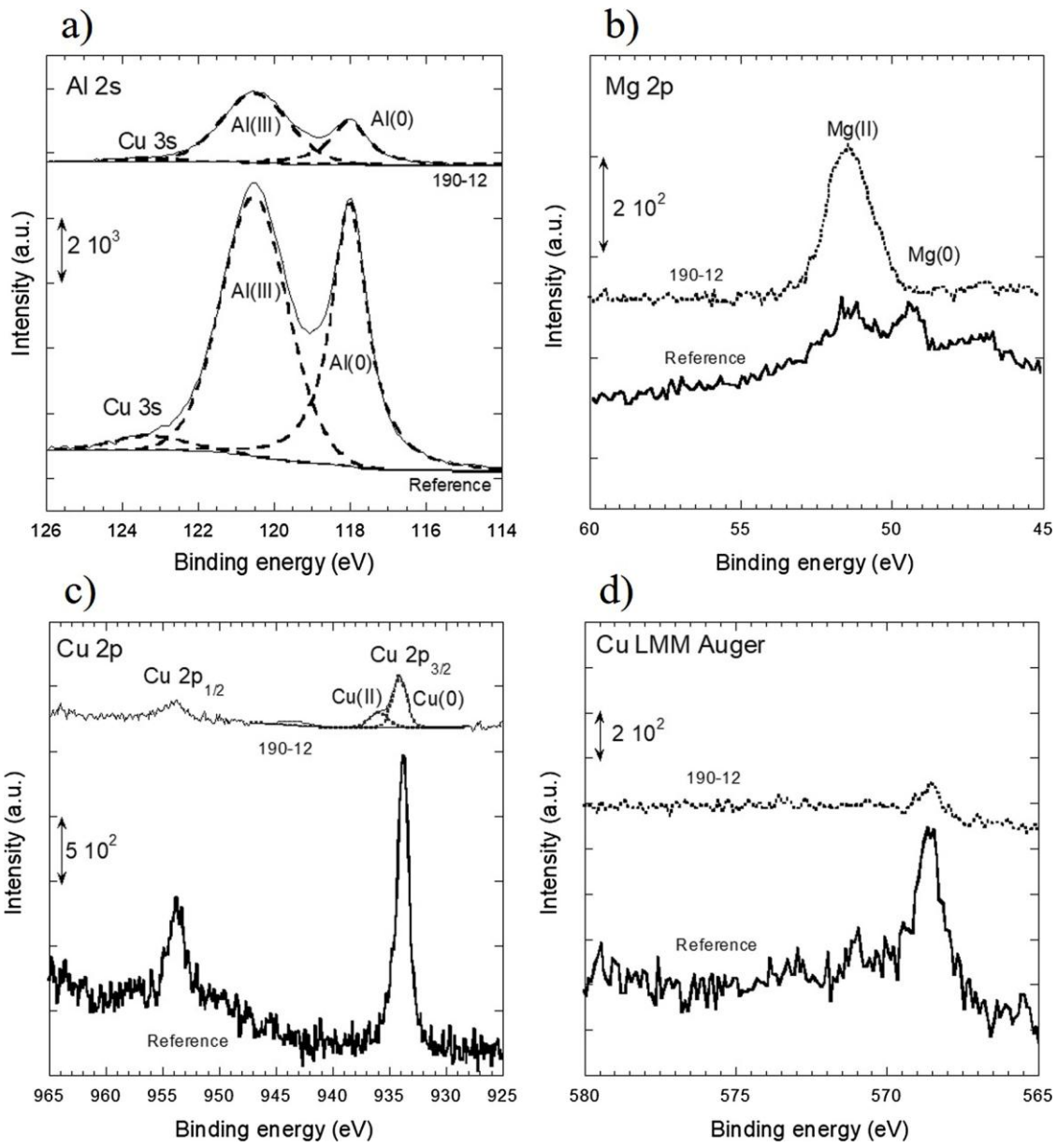

Fig. 3. XPS a) Al 2 s, b) Mg 2p, c) Cu 2p spectra and d) Cu LMM Auger spectra for the Reference and 190-12 samples.

overestimation of the minimum oxide thickness.

The effect of the thermal treatment on the composition and structure of the oxide layer was then studied. Fig. 2b shows the same ions (AlO_2^-, Al_2^-, Cu^-, CuO^-, MgO^-) for the thermally treated sample (190−12) as for the Reference sample. The 190-12 sample is also characterised by distinct regions: the oxide, the intermediate and the bulk regions.

The shape of the ion depth profiles is similar to the Reference sample, except for the MgO^- profile (Fig. 2b), which shows a significant intensity increase, of almost 10 orders of magnitude, in the oxide and intermediate regions as compared to the intensity observed for the Reference sample (Fig. 2a). This intensity increase is related to a significant enrichment of the thermal Al oxide layer in Mg oxide induced by the thermal treatment at 190 °C during 12 h. The surface enrichment in Mg oxide has already been observed on thermally treated Al-Mg alloys (AA5657, AA5252, AA7175 or AA7075) [58–61]. The similar shapes of the MgO^- and AlO_2^- signals in the oxide layer suggest a homogenous in-depth distribution of these two oxides. The MgO^- signal intensity decreases slightly faster than AlO_2^- signals in the intermediate region and reaches a stable intensity in the bulk region corresponding to a similar value as the one observed for the Reference sample. Similarly to the Reference sample, the Al_2^- and Cu^- signals show low intensity in the oxide region and then a steep increase is observed in the intermediate region. The shapes of the CuO^- and Cu^- signals are similar for the Reference and 190-12 samples, but their intensities in the intermediate region are slightly higher for the 190–12 sample, indicating slightly stronger Cu enrichment at the oxide/alloy interface for the 190–12 sample. It should be noted here that a possible enhanced ionisation yield at interfaces between matrices (especially between oxide and metallic matrices) cannot be excluded. Nevertheless, the combination of ToF-SIMS and XPS analyses (see results below), as well as previous work [57], strengthen the conclusion that the Cu^- and CuO^- signals indicate Cu enrichment at the oxide/alloy interface. The slightly higher intensity of the CuO^- signal at the oxide/alloy interface for the 190–12 sample could be explained by an additional contribution of the numerous intergranular Cu-rich precipitates (Fig. 1d), which can be partially oxidised at their surfaces, as observed for Cu-rich IMCs [57].

Another significant difference between the Reference and 190—12 samples is observed in the sputtering time. For the 190—12 sample, the

oxide (~11 s) and the intermediate region (~35 s) show longer sputtering times in comparison to the Reference sample, indicating the thickening of the oxide layer as well as the increased roughness. Considering that the oxide formed on both samples was mainly composed of Al oxide, the differences in surface chemical composition were assumed not to contribute to the differences in sputtering times. The minimum and maximum oxide thicknesses for the 190–12 sample were evaluated to 4 and 13 nm, respectively, as indicated in Fig. 2b (top axis).

Fig. 3 shows Al 2 s, Mg 2p, Cu 2p core levels and the Cu LMM Auger line obtained for Reference and 190–12 samples, recorded in order to determine the chemical composition of the surface.

The Al 2 s (Fig. 3a) core level was used since in the Al 2p region there is an overlap of Al 2p signal with Cu 3p [56]. The lower binding energy peak at 117.7 eV in the Al 2 s region can be assigned to the metallic Al and the higher binding energy peak at 120.0 eV to the oxidised Al(III), in agreement with literature [62]. Metallic and oxidised components are observed for both the Reference and 190–12 samples, indicating the formation of thin oxide layers at least in some areas of the surface. Only one symmetrical peak is observed at 51.4 eV in the Mg 2p core level for the 190–12 sample (Fig. 3b), corresponding to the oxidised Mg, whereas for the Reference sample two peaks are observed, one metallic Mg signal at a binding energy of 49.7 eV, and that of oxidised Mg at a binding energy of 51.4 eV [63,64]. Fig. 3c shows the XPS Cu 2p peak for the Reference and 190—12 samples. The Cu 2p core level spectrum shows characteristic spin-orbit splitting for Cu $2p_{3/2}$ and Cu $2p_{1/2}$ with ΔBE = 19.75 eV. For simplicity, only one peak (Cu $2p_{3/2}$) was decomposed. For the Reference sample, the Cu $2p_{3/2}$ peak shows one component at 933 eV, whereas for the 190–12 sample, two peaks at 933 eV and 935 eV can be observed. The analysis of the Cu LMM Auger spectra (Fig. 3d) was necessary in order to identify the chemical nature of Cu present on the surface. The calculation of the modified Auger parameter α′ (α′ = BE (Cu $2p_{3/2}$) KE (Cu LMM) 933.0 eV 918.3 eV 1851.3 eV) indicates the presence of metallic Cu [65] for the Reference sample. The binding energy of Cu $2p_{3/2}$ for a pure metallic Cu is expected at 932.6 eV. In AA2024, Cu is essentially present in intermetallic particles composed of several alloying elements. Literature data showed a binding energy positive shift for bimetallic systems, e.g. Al_2Cu particles, with reference to pure metal [66,67]. In the case of 190–12 sample, the presence of metallic Cu was also confirmed and the higher binding energy peak at 935 eV was attributed to $Cu(OH)_2$.

In first approximation, assuming a continuous and homogeneous oxide/hydroxide layer on top of the alloy substrate, the compositions of the underlying substrate (corresponding to metallic species) and of the oxide/hydroxide layers were estimated (Table 1).

For the Reference and 190–12 samples, the underlying alloy was enriched in Cu as compared to the nominal composition of the alloy, i.e. 1.9 at. % of Cu. The enrichment was the same for both samples. No oxidised Cu was detected at the surface of the Reference sample and only 0.2 at. % at the surface of the 190—12 sample. The detection of oxidised Cu for the 190—12 sample was in agreement with the higher CuO^- signal as compared to the Reference sample. Concerning Mg signals, the Mg amount in the underlying alloy was slightly lower than the nominal composition (1.6 at. %) for the Reference sample, and no Mg was detected in the underlying alloy for the 190–12 sample. Therefore, the results showed that the underlying alloy was depleted in Mg, particularly for the 190–12 sample. An enrichment in Mg was observed in the oxide/hydroxide layer for both samples. This enrichment was low for the Reference sample (2 at. %) as compared to the nominal composition of the substrate and significantly stronger for the 190–12 sample (19.2 at. %), which was in agreement with ToF-SIMS results. The enrichment in Mg of the oxide/hydroxide layer is responsible for the Mg depletion of the underlying alloy, especially for the 190–12 sample. These results could be explained by previous data reported in literature.

Seyeux et al. reported that a pure Al oxide layer is formed above both the Al_2Cu particles and the matrix, and observed localised enrichment of metallic Cu at the metal/oxide interface [68]. Similarly, segregation of metallic Cu and Ag at the metal/oxide interface was observed for thermally-treated Al-Cu-Li alloy, with an oxide film composed mainly of Al and Li oxides [69]. Thompson et al. [70–74] showed a uniform layer composed of alumina formed on Al-Cu model alloys, but a thin Cu layer was also observed at the oxide/Al alloy interface. However, Zhou et al. [74] also found Cu oxides in the anodic film formed on an Al-2 wt. % Cu alloy. Thus, as demonstrated in the literature, the presence of Cu oxides in the alumina film depend on the amount of metallic Cu in the Al-Cu alloy and the oxidation conditions. Based on previous findings, it could be proposed in the current study that the oxide film formed on the matrix was mainly composed of alumina for both samples. The Cu enrichment in the underlying alloy was associated with the oxidation of the Cu-rich solid solution, i.e. the matrix, with similar Cu enrichment of the underlying alloy for both samples. The presence of Cu in the oxide film could be related to Cu-rich precipitates. For the Reference sample, oxidation of the Cu-rich IMCs could lead to the increased intensity of the CuO^- signal at the oxide/alloy interface in agreement with Cornette [57], but the amount of Cu oxides was not sufficient to be detected at the sample surface by XPS. For the 190–12 sample, the contribution of the numerous Cu-rich intergranular precipitates should allow Cu species to be detected in the oxide film. The presence of Mg in the oxide film could be assigned to the oxidation of the Mg-rich matrix, but also Mg-containing precipitates (both IMCs and intergranular precipitates). We showed in previous study [75] that the passive film grown on Al–Cu–Mg alloy contained Cu species, but it was also enriched with Mg due to the high diffusion rate of Mg through the alumina film [76]. The differences between the Reference and the 190–12 samples could be explained by the thermal treatment at 190 °C which promotes Mg diffusion, in agreement with literature [58–61], and the higher amount of intergranular Al_2CuMg precipitates for the 190–12 samples.

The measurement of oxide thickness is often done by XPS, using the attenuation of the signal from the metallic substrate by a thin surface oxide layer. However, the XPS signal is recorded from an analysed area on which patches of thicker oxide can co-exist with a thin oxide/hydroxide layer, while the calculation would consider a layer of uniform thickness. The calculation also assumes a smooth surface and a sharp interface, which is not the case here (the surface is rough, as shown above). However, the Al(III)/Al(0) intensity ratio for the 190–12 sample is higher than on the Reference sample (Fig. 3a) indicating a thicker oxide layer on the 190—12 sample. The increase of oxide thickness on the thermally treated sample was evidenced by ToF-SIMS (minimum oxide thickness layer of 2 nm for the Reference sample and 4 nm for the 190–12 sample). This is consistent with the ageing treatment at 190 °C for 12 h leading to Al oxidation and growth of the oxide layer.

To sum up, the results showed that the ageing treatment at 190 °C for 12 h led to a significant modification of the microstructure with the precipitation of the S-Al_2CuMg phase and/or intermediates of S-phase, i.e. S′-phase, at the grain boundaries and inside the grains. In addition, during the ageing treatment, the oxide layer thickened and became enriched with Mg, leading to a significant depletion in Mg in the

Table 1
Analysis of the surface composition for the Reference and the 190-12 samples, before and after degreasing and deoxidation. ND: non-detected.

		Before pre-treatment			After degreasing and deoxidation		
Composition (at. %)		Al	Cu	Mg	Al	Cu	Mg
Reference	Metallic species (underlying alloy)	96.0	3.0	1.0	83.3	16.7	ND
	Oxide/hydroxide	98.0	0.0	2.0	99.0	1.0	ND
190—12	Metallic species (underlying alloy + deposits)	97.0	3.0	0.0	77.1	22.9	ND
	Oxide/hydroxide	80.6	0.2	19.2	99.0	1.0	ND
Nominal composition		96.5	1.9	1.6	96.5	1.9	1.6

underlying alloy for the 190–12 sample. The presence of Cu(II) was evidenced in the oxide layer of the 190–12 sample and a Cu enrichment of the underlying alloy was shown; for the reference sample, only Cu enrichment of the underlying alloy was observed. These differences in surface composition of the two samples likely have an influence on their reactivity in the degreasing and deoxidation baths.

3.2. *Surface characterisation of the degreased and deoxidised samples*

3.2.1. *ToF-SIMS and XPS analyses of the degreased and deoxidised surfaces*

Fig. 4 shows the characteristic negative ion depth profiles obtained for the Reference and 190–12 samples following the alkaline degreasing and acidic deoxidation steps, during which the oxide layers discussed above were dissolved and new oxide layers were formed. Similarly to the results obtained before the degreasing and deoxidation, three characteristic regions can be distinguished for both samples, i.e. oxide, intermediate region and bulk sample region. However, for both samples, a longer sputtering time for the oxide region is observed after degreasing and deoxidation: ~40 s *vs* ~5 s for the Reference sample (Fig. 2a and Fig. 4a, respectively), and 80 s *vs* ~11 s for the 190–12 sample (Fig. 2b and Fig. 4b, respectively). The increase of sputtering time is also observed for the intermediate region, and the substrate regions for both samples after degreasing and deoxidation. It can be explained not only by the growth of a thicker oxide layer but also by the surface roughening induced by the pre-treatment. The larger increase in the sputtering time observed for the 190–12 sample may be explained by a more significant increase in the oxide thickness as compared to the Reference sample. Another explanation is a rougher surface for the 190–12 sample, which is confirmed by AFM measurements presented below. The higher roughness can be also recognized by the slow increase and decrease of the ion intensity signals. More particularly the degreased and deoxidized 190—12 sample (Fig. 4b) shows slow signal intensity changes in the intermediate region, i.e. AlO_2^-, CuO^-, Cu^- decrease and Al_2^- increase. As previously explained, the oxide thickness was calculated using the sputtering rate for the native oxide measured for the Reference sample. Despite this hypothesis, neglecting possible effects of the chemical composition of the oxide on the sputtering rate, and the surface roughness, it is thought that the maximum oxide layer thickness of ~ 30–90 nm for the degreased and deoxidised 190—12 samples, as compared to ~ 15–40 nm for the degreased and deoxidised Reference sample (top axes in Fig. 4b and a, respectively) is meaningful.

Considering that the process of degreasing and deoxidation introduces some changes in the chemical composition of the newly formed oxide layers, attention was then paid to the chemical composition of the surface. In the oxide region for both samples, the MgO^- signals appear lower than before the pre-treatment, which could be related to a dissolution of Mg oxide/hydroxide during the degreasing and deoxidation steps. The most significant difference is observed for the 190–12 sample where a significant Mg enrichment of the oxide film had been observed due to thermal treatment (Fig. 2b), and then a dissolution after degreasing and deoxidation (Fig. 4b). For this sample, the MgO^- signal has an intensity almost four orders of magnitude lower after the degreasing and deoxidation with respect to the sample before the pre-treatment (Fig. 2b and 4b).

The Cu^- and CuO^- signals are also modified. The intensity increase of both Cu^- and CuO^- signals in the oxide and intermediate regions (Fig. 4) with respect to the samples before the pre-treatment (Fig. 2) suggests a Cu enrichment. For the degreased and deoxidized Reference sample (Fig. 4a), clearly two distinct maxima for the Cu^- and CuO^- signals can be observed i.e., one after a 30 s sputtering, and another one after 85 s sputtering, in the oxide and at the intermediate region/substrate interface, respectively. Thus, this Cu signal indicates the Cu enrichment in the oxide layer, and also at the interface between the metallic substrate and the oxide layer. For the degreased and deoxidized 190–12 sample (Fig. 4b), the Cu^- signal is less well resolved due to the higher roughness of the samples, but the rapid increase in the oxide and a high intensity in the intermediate region can be observed. When comparing the Reference (Fig. 4a) and 190—12 (Fig. 4b) samples after degreasing and deoxidation, a stronger Cu-enrichment (higher CuO^- signal) in the oxide and in the intermediate region can be observed for the 190–12 sample than for the Reference sample. Due to the roughness of the samples induced additionally by the degreasing and deoxidation, and the ToF-SIMS analysis performed at 45° to the sample surface for the sputtering and analysis, it is difficult to conclude about the structure of the oxide and the presence of metallic and oxidised Cu species. The analysis will be then supported by the XPS characterization presented in the following part. However, based on the ToF-SIMS ion depth profile and despite the lack of accuracy linked to the increased roughness, it can be concluded that for both samples the oxide layer formed after

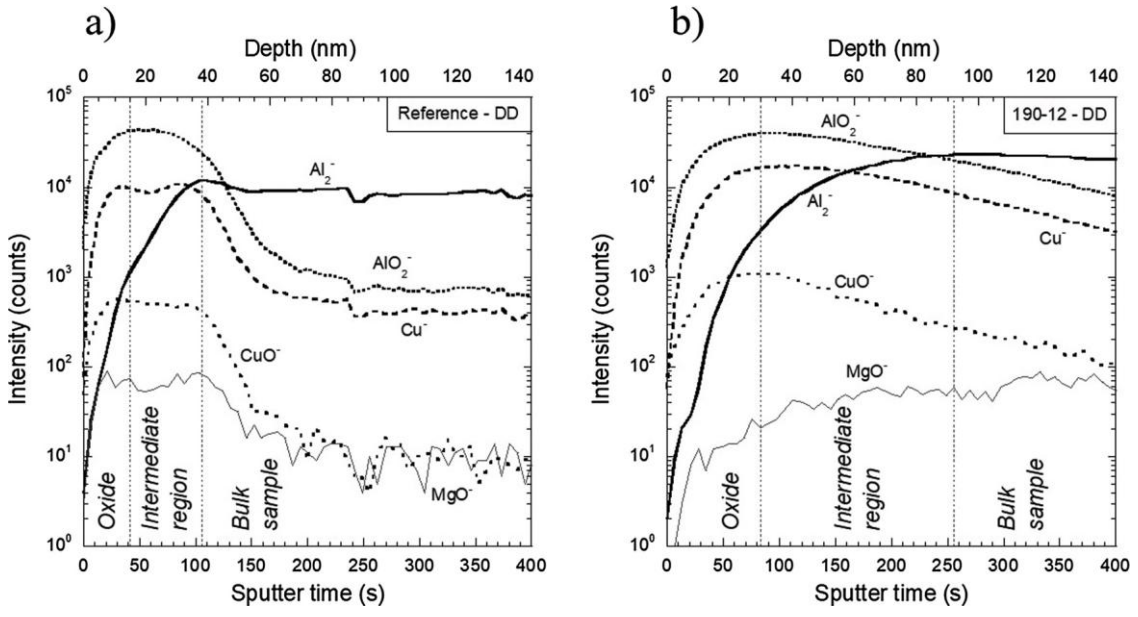

Fig. 4. ToF-SIMS negative secondary ion depth profiles: AlO_2^-, Al_2^-, Cu^-, CuO^-, MgO^- obtained for a) the reference AA2024-T3 sample (Reference) and b) the AA2024-T3 sample thermally treated at 190 °C during 12 h (190-12), after degreasing and deoxidation (DD).

degreasing and deoxidation is thicker than before the pretreatment. Furthermore, for both samples, a Cu enrichment was observed in the oxide and in the intermediate region due to the pre-treatment, with a more marked Cu enrichment for the degreased and deoxidised 190–12 sample than for the degreased and deoxidised Reference sample. Finally, for both degreased and deoxidised samples, the MgO^{-} amount was negligible.

Fig. 5 shows Al 2 s, Mg 2p, Cu 2p core levels and the Cu LMM Auger line obtained for degreased and deoxidised Reference and 190–12 samples. It is interesting to note here that Fe was not detected by XPS for both samples, meaning that the Fe concentration was lower than 1 at.% at the sample surface, even if some authors showed that, by using Fe-based deoxidisers, Fe-deposits could form [77]. The results here are in agreement with ToF-SIMS analyses, where Fe species (Fe^{-} or FeO^{-}) have not been detected for both the 190–12 and Reference samples after degreasing and deoxidation.

The XPS Al 2 s spectra of the degreased and deoxidised Reference and 190—12 samples (Fig. 5a) are quite similar with a low binding energy component associated to Al(0) and a high binding energy component associated to Al(III). The Al(0) component is still detected meaning the presence of areas with a locally thinner oxide/hydroxide layer (thinner than 10 nm). However, as discussed above, ToF-SIMS data have indicated that the minimum oxide thickness is 15 nm and 30 nm for the degreased and deoxidised Reference and 190–12 samples, respectively. The evaluation of the oxide thickness is affected by the strong sample roughness and the analysis angle by ToF-SIMS. Moreover, the calibration of the sputtering rate was performed only on the Reference sample and used for calculation for all samples, which can also introduce some error in the oxide thickness estimation, as previously mentioned. Nevertheless, despite these approximations, the oxide layers are clearly thicker after the pre-treatment for both samples. This is in agreement with the increase in the intensity ratio Al(III)/Al(0) after pre-treatment for both samples. Therefore, it can be concluded that the most relevant hypothesis to explain the results is that the oxide layers were not homogeneous in thickness, leading to the presence of the Al(0) component.

The Mg 2p signal (Fig. 5b) shows a very weak signal of similar

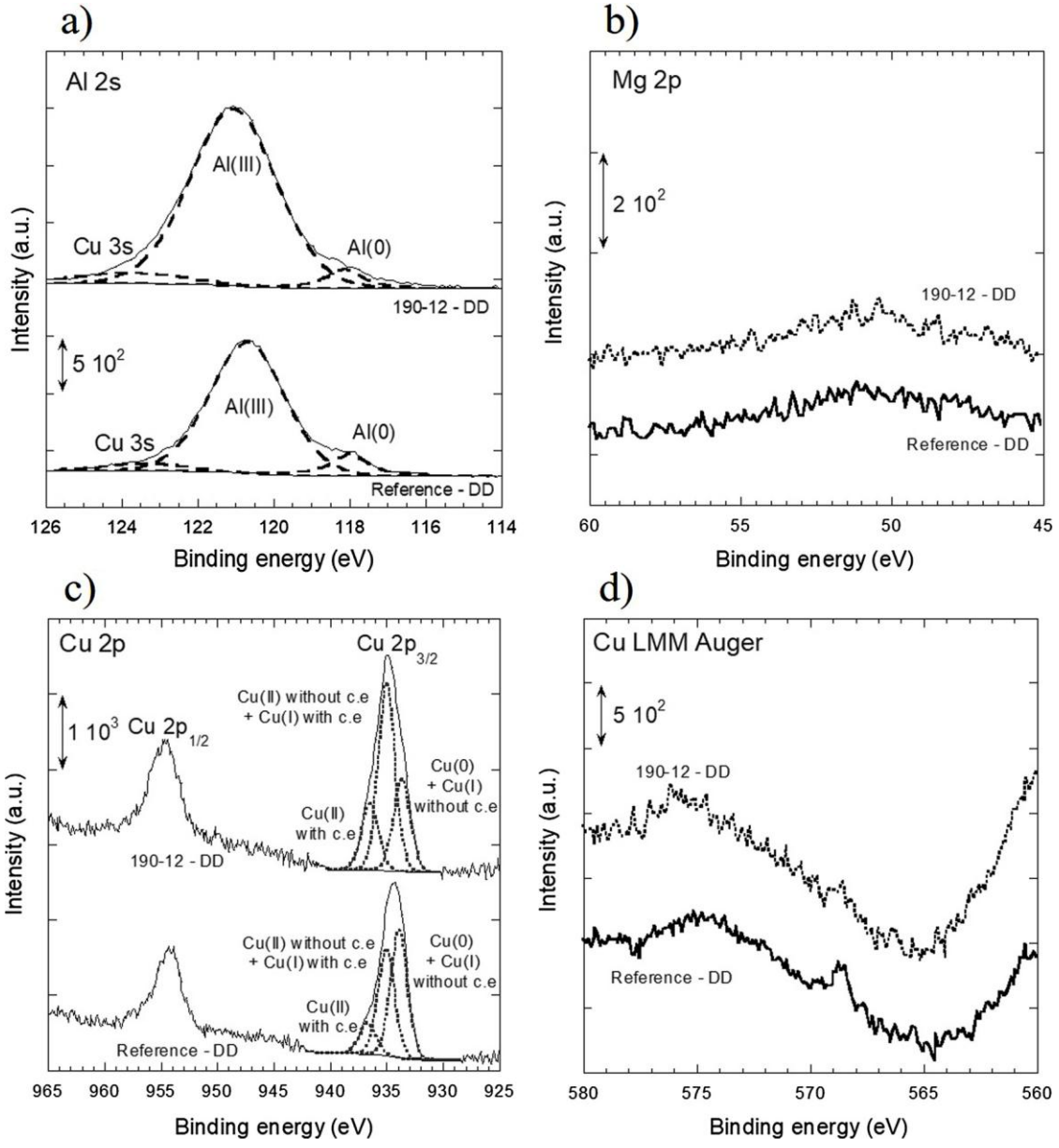

Fig. 5. XPS a) Al 2 s, b) Mg 2p, c) Cu 2p spectra and d) Cu LMM Auger spectra for the Reference and 190-12 samples after degreasing and deoxidation. c.e.: charging effect.

intensity for both samples. This result indicates the dissolution of Mg oxide for both samples, and also the dissolution of metallic Mg in the underlying alloy for the Reference sample. The dissolution of the oxide can be explained by the chemical aggressiveness of the pre-treatment baths.

The spectra of the Cu 2p core level are reported in Fig. 5c for the degreased and deoxidised Reference and 190–12 samples. For both samples, three Cu peaks can be associated to Cu(0) (933 eV), Cu(II) in hydroxide (935.8 eV), and the third peak at 934.2 eV may be attributed to Cu(II) and/or Cu(I) redeposited at the surface. Cu(I) peak should be observed at 932.8 eV, but taking into account the shift due to electrostatic charging (1.6 eV according to the C 1s peak shift), its binding energy is expected at 934.4 eV. The metallic Cu concentrations after degreasing and deoxidation were 22.9 at. % and 16.7 at. % for the degreased and deoxidised 190–12 and Reference samples, respectively. For comparison, it was 3 at. % for the two samples before degreasing and deoxidation (Table 1). These values are upper values as they are obtained assuming that metallic Cu is located under an oxide layer, which thickness is overestimated. The Cu(0) signal can be attributed to the metallic Cu present in the alloy substrate locally covered by a thin oxide layer. However, the Al(III) signal originates from the whole analysed surface area including the thin and the thick oxide layers. These results show therefore that the degreasing and deoxidation lead to Cu enrichment of the underlying alloy for both samples. Moreover, the Cu content in the underlying alloy was found to be higher for the 190–12 sample than for the Reference sample, after the pre-treatment. However the presence of metallic Cu deposits formed during degreasing and deoxidation due to the removal of Cu-rich intermetallics [32–34] cannot be excluded. For the oxide/hydroxide film formed after degreasing and deoxidation, a similar Cu content of ~ 1 at. % was measured for both samples. This value is higher than the one measured for the oxide films formed before the pre-treatment (0 at. % and 0.2 at. %, for the Reference and the 190–12 samples, respectively). Thus, the XPS data clearly confirm the Cu enrichment observed already by ToF-SIMS.

The strongly non-uniform layer thickness and the surface roughness after the pre-treatment made the estimation of the oxide thickness difficult. However, the higher Al(III)/Al(0) intensity ratio for the 190–12 sample than for the Reference sample after degreasing and deoxidation indicates a thicker oxide/hydroxide layer on the 190–12 sample, in agreement with ToF-SIMS data.

3.2.2. *Focus on the surface Cu enrichment and roughness*

To complete previous surface analysis, cyclic voltammetry (CV) tests were performed following the method described in literature [32–34]. Fig. 6a shows the CV curves in the area of the peak corresponding to the Cu oxidation from Cu(0) to the Cu(I) for the Reference sample before, and after degreasing and deoxidation. The same CV test was also performed for a pure Cu sample (not shown). The surface area of this anodic peak for different samples was measured and then, the electroactive Cu coverage (θ_{Cu}) of the surface was determined by using Eq 1 [32]:

$$\theta_{Cu}(\%) = \frac{\text{Area under Cu(0) to Cu(I) peak of studied samples}}{\text{Area under Cu(0) to Cu(I) peak of pure Cu}} \times 100 \qquad (1)$$

Values of θ_{Cu} for the Reference and 190–12 samples before and after the pre-treatment stage are presented in Fig. 6b. Before the pre-treatment, θ_{Cu} was lower for the 190–12 sample than for the Reference sample. This result could be explained by the presence of a thick oxide on the 190–12 sample due to the ageing treatment, which was described in details earlier in the manuscript (Fig. 2). Then, for both samples, θ_{Cu} increased after the pre-treatment; moreover, θ_{Cu} became higher for the 190–12 sample than for the Reference sample.

SEM images obtained for the Reference sample after degreasing and deoxidation show that Cu-rich IMCs have been removed during the pre-treatment step (Fig. 7a), as well as some dispersoids (Fig. 7b). The images also show a specific surface morphology of the Al alloy after pre-treatment, commonly called scalloped surface (Fig. 7c): it is a typical feature of electropolished and chemically polished aluminium alloys characterised by ridges and troughs, and explained by the interactions between residual impurities and alloying elements [78]. The same observations were also done for the 190–12 sample after the pre-treatment. Further AFM measurements showed a rough surface for both the Reference (Fig. 8a) and 190–12 samples (Fig. 8b), confirming the strong dissolution inside the grains followed by the growth of the scalloped surface as shown above. It could be also noted that the roughness of the 190–12 sample was twice that of the Reference sample. In addition, AFM observations of the 190–12 sample surface (Fig. 8b) clearly showed a strong dissolution of the grain boundaries, which was not observed for the Reference sample (Fig. 8a).

3.2.3. *Correlation between microstructure and chemical composition of the surface*

During the degreasing and deoxidation, the dissolution of the Cu-rich

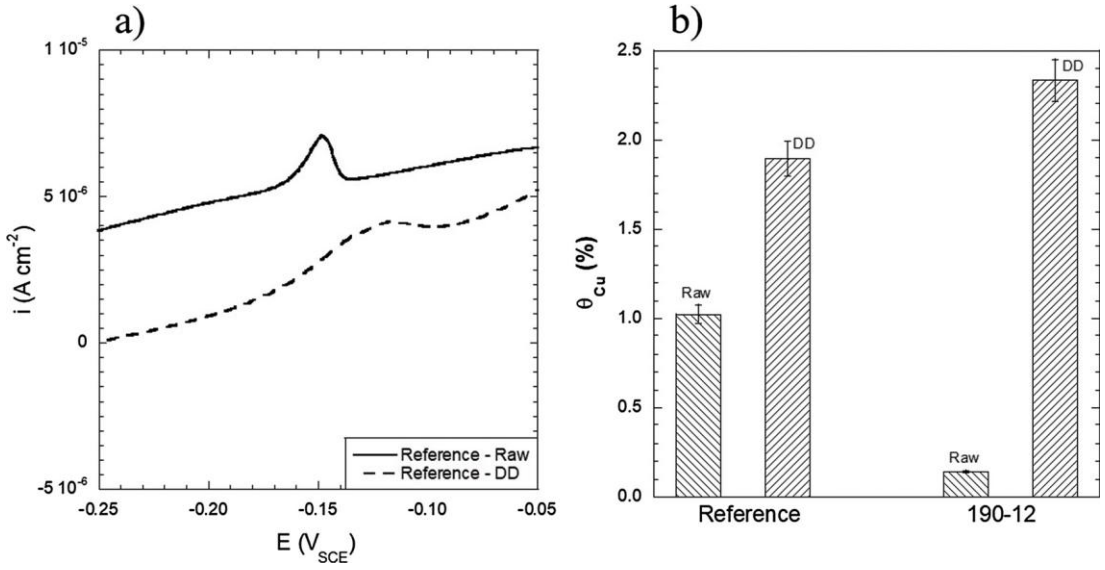

Fig. 6. a) Cyclic voltammetry curves for the Reference sample before and after degreasing followed by deoxidation pre-treatment and b) surface Cu coverage calculated from CV curves for the Reference and the 190-12 samples before and after degreasing followed by deoxidation.

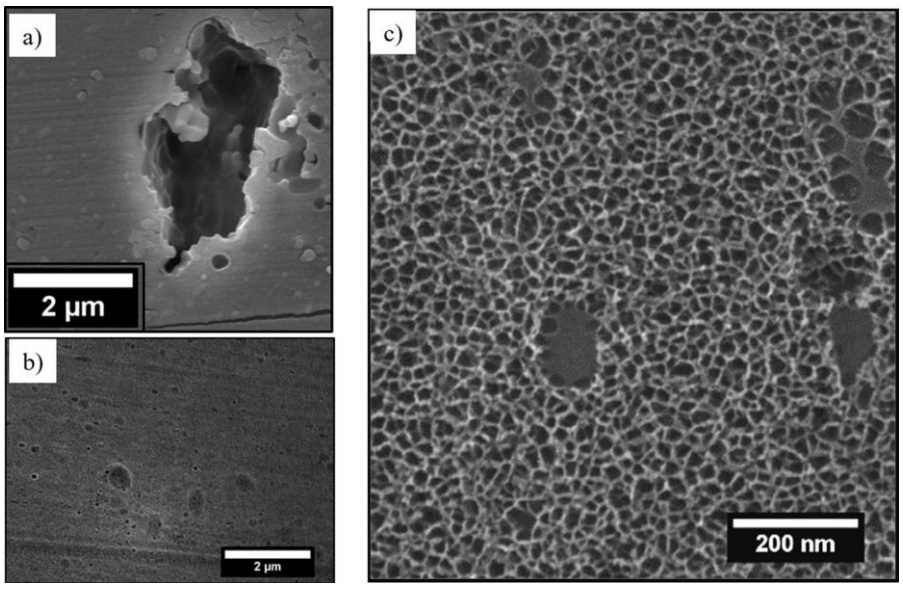

Fig. 7. Characterisation of the surface morphology of the Reference sample after degreasing and deoxidation. SEM image showing the removal of a) Cu-rich IMCs, and b) some dispersoids; c) SEM image showing the scalloped surface.

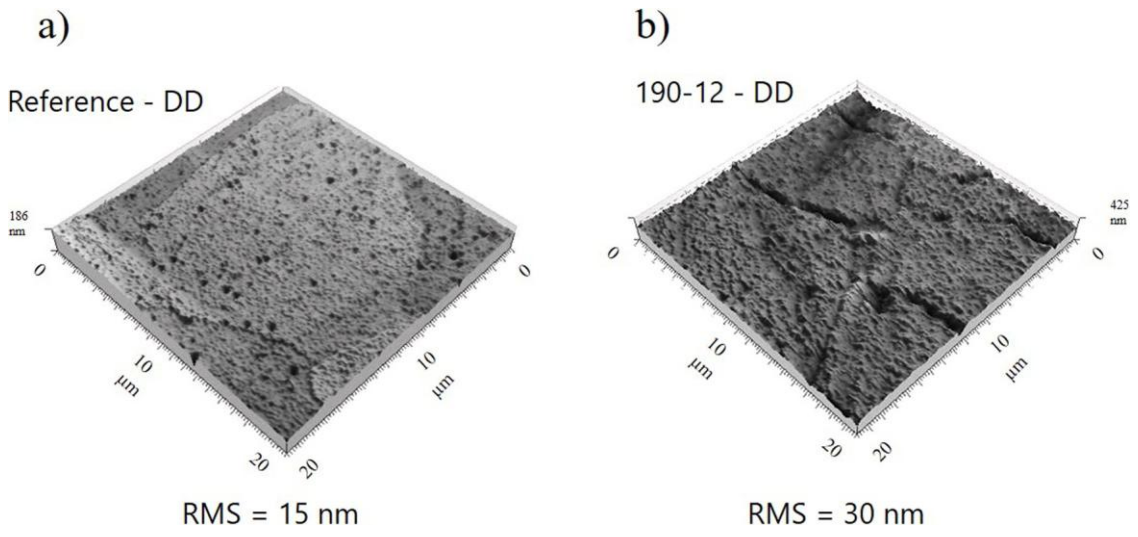

Fig. 8. AFM maps (20 × 20 µm^2) in topographical mode for the Reference sample (a) and 190-12 sample (b) after degreasing and deoxidation.

Al matrix occurred [77,79,80]. Harvey et al. described a three-stage model to explain the acid deoxidation of aluminium alloys [79], with in the second stage the dissolution of the aluminium matrix that leaved behind an accumulation of Cu in agreement with other authors [78,81], and then, in the third stage, the establishment of an equilibrium between dissolution and growth of the oxide film. This led to the formation of an alumina film on the Cu-rich solid solution after acid deoxidation with Cu accumulated at the oxide/metal interface. The authors also showed that Cu accumulation could be due to either the Cu-rich solid solution or to Cu-rich hardening precipitates. These results are in agreement with Ralston et al. [82] who showed that the intragranular nanoscale Cu-rich precipitates were also involved in electrochemical reactions. Therefore, the Cu enrichment in the underlying alloy shown here in this work by ToF-SIMS and XPS analyses for the Reference sample can be attributed to the Cu-rich solid solution, whereas Cu-rich hardening precipitates should be also considered for the 190–12 sample. Furthermore, galvanic couplings at the nanometre scale between those precipitates and the Cu-rich solid solution leading to a higher roughness of the grains for the 190–12 sample than for the Reference sample (as demonstrated by AFM, Fig. 8b) should also be taken into account. This does not mean that the morphology of the features observed by AFM topographical maps is directly associated with hardening precipitates, as the size of those features is not in line with the size of those precipitates. It cannot be excluded also that the dissolution of both the Cu-rich solid solution and the Cu-rich hardening precipitates combines with the formation of some Cu deposits. Therefore, considering that all Cu detected by CV measurements could be attributed to either Cu deposited on the alloy surface or Cu-containing intermetallics as indicated by Scully [32], it can be assumed that the dissolution of the Cu-rich solid solution for both the Reference and 190−12 samples contributed to the increase in θ_{Cu} after degreasing and deoxidation, whereas the contribution of the Cu-rich intergranular precipitates had to be considered for the 190–12 sample. Nevertheless, considering that the formation of Cu-rich intergranular precipitates led to a Cu depletion of the solid solution, no

changes in the global amount of Cu at the oxide/metal interface should be observed between the Reference and 190–12 samples, whereas previous XPS analyses showed a Cu amount of 16.7 at. % and 22.9 at. % in the underlying alloy for the Reference and 190–12 samples, respectively. This should be explained by keeping in mind that Cu was considered as part of the underlying alloy when it was analysed as metallic Cu. It is of importance to note here that metallic Cu could be also attributed to Cu deposits present at the sample surface, or Cu remnants from Cu-rich IMCs or Cu-rich intergranular precipitates. As mentioned above, the dissolution of both the Cu-rich solid solution and Cu-rich intergranular precipitates could lead to Cu redeposition. However, for the Reference sample, it was assumed that most part of the Cu deposits were due to the removal of Cu-rich IMCs (Fig. 7a), followed by Cu redeposition, which contributed significantly to the increase in θ_{Cu} after degreasing and deoxidation. The differences in θ_{Cu} after degreasing and deoxidation between the Reference and 190–12 samples is likely related to the reactivity of the Cu-rich intergranular precipitates, more numerous and coarser after the ageing treatment at 190 °C (Fig. 1d). Those precipitates could also be associated with dissolution processes followed by Cu redeposition, in agreement with the roughness observed at the grain boundaries in the AFM topographical maps (Fig. 8b) for the 190—12 samples. Therefore, the reactivity of Cu-rich intergranular precipitates can explain the higher θ_{Cu} after degreasing and deoxidation for the 190–12 sample as compared to the Reference sample. This could also, at least partially, explain the higher metallic Cu amount detected by XPS for the 190–12 sample, considering, as said above, that Cu in metallic form is assigned, after degreasing and deoxidation, to both Cu in the underlying alloy as a Cu-rich layer and as Cu deposits from Cu-rich IMCs and Cu-rich intergranular precipitates. This comment is also in agreement with the higher Cu^- signal in the oxide region of the ToF-SIMS in-depth profile after degreasing and deoxidation as compared to the signal before this pre-treatment for both samples, and with the higher Cu^- signal in the oxide region for the 190–12 sample as compared to the Reference sample. It is also noted that Cu deposits as well as Cu-rich IMC/Cu-rich intergranular precipitates remnants could be partially oxidised at their surface because of the high concentrations

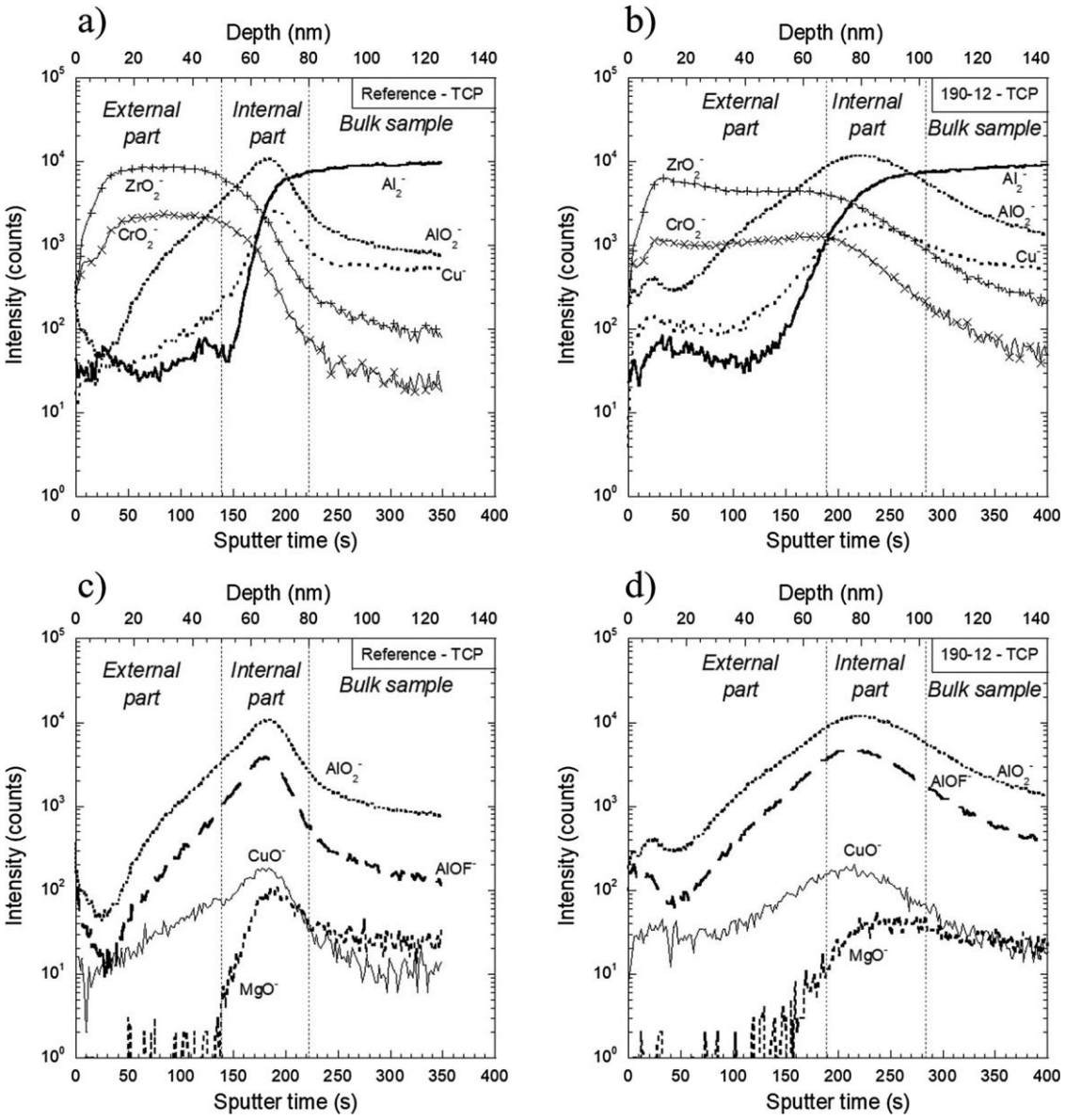

Fig. 9. ToF-SIMS negative secondary ion depth profiles: AlO_2^-, Al_2^-, Cu^-, ZrO_2^- and CrO_2^- obtained for the TCP coated samples a) the reference AA2024-T3 sample (Reference) and b) the AA2024-T3 sample after thermal treatment at 190 °C during 12 h (190-12). Figures c) and d) show the AlO_2^-, CuO^-, MgO^- and $AlOF^-$ depth profiles for the same samples.

in alloying elements [78,79,81]. The exact conditions in which copper is oxidised are not elucidated, but this could explain the higher amount of oxidised Cu in both the Reference and 190–12 samples after degreasing and deoxidation as compared to the analyses before this pre-treatment. Finally, AFM analysis confirmed the previous description of the sample surface established on the basis of ToF-SIMS results with a surface characterized by a strong roughness after degreasing and deoxidation for the 190–12 sample, which had been taken into account in the description and interpretation of the ToF-SIMS results. All these peculiarities of the surface after degreasing and deoxidation observed for the 190-12 sample, with in particular a strong surface roughness and a Cu enrichment, could be detrimental for the growth of the TCP coating.

3.3. *Characterisation of the coated samples*

3.3.1. *Chemical composition and structure of the TCP coating*

Fig. 9 shows the characteristic ToF-SIMS negative ion depth profiles obtained on TCP coated Reference and 190–12 samples, recorded in order to determine the chemical composition and structure of the TCP coating. As previously done for the samples before and after degreasing and deoxidation, Cu^-, Al_2^-, CuO^-, AlO_2^- and MgO^- ion signals are shown. The additional signals shown here such as ZrO_2^-, CrO_2^- are characteristic of the external part of the TCP coating and $AlOF^-$ the internal part of the TCP coating. Indeed, as indicated in the literature, the TCP coating is often present as a bi-layer coating, including an internal part rich in Al oxide and Al fluorides, acting as a barrier layer, and related to the fluoride attack of Al in the conversion bath [30,83–85], and an external part rich in Zr and Cr oxides and hydroxides [24,26,56,86,87]. Three main regions can be identified for both samples as a function of the intensity changes of the signals corresponding to the metallic substrate (Cu^-, Al_2^-) and to the TCP coating (ZrO_2^-, CrO_2^- and $AlOF^-$): external part and internal part of the TCP coating first, and then the bulk sample region. The three regions are marked in Fig. 9 by vertical dashed lines.

The intensities of ZrO_2^- and CrO_2^- signals in Fig. 9a and b remain high until 140 s and 190 s for the Reference and 190–12 samples, respectively, suggesting a thicker external part of the TCP coating for the 190–12 sample. Similarly, the intensities of AlO_2^- and $AlOF^-$ signals, which increase when probing deeper than the external part, remain high until 220 and 280 s for the Reference and 190—12 samples, respectively. For longer sputtering times, the Al_2^- signal reaches a plateau indicating the position of the metal/oxide interface. The metallic substrate is observed after longer sputtering time for the 190–12 sample than for the Reference sample. The main difference in thickness for the 190-12 sample, as compared to the Reference sample is assigned to the modification of the external Cr and Zr rich oxide, the thickness of the inner Al oxide remaining similar. However, similarly to what was observed for the degreased and deoxidised 190-12 sample, the global shape of the signals suggests that the longer sputtering times for the TCP coated 190–12 sample can be also related to surface roughness induced by the degreasing and deoxidation steps. The intensities of both Cu^- and CuO^- signals were similar for the TCP coated Reference and 190–12 samples, with a slower decrease of the signals for the 190-12 samples, probably related to a rougher surface. The MgO^- signal is very weak in the external part for both samples; however a significant increase can be observed in the internal part, indicating a Mg oxide enrichment at the TCP/alloy substrate interface.

SEM-FEG observations of cross-sections of the TCP coatings formed on both the Reference and 190—12 samples are shown in Fig. 10. The thickness of the TCP coating was estimated to 127 and 223 nm for the Reference and 190–12 samples, respectively. Such an increase in the TCP coating thickness for the 190–12 sample with respect to the Reference sample is in agreement with ToF-SIMS results. Moreover, SEM-FEG observations clearly showed that the TCP coating formed on the 190-12 sample was less adherent to the substrate than that formed on the Reference sample, with a stronger roughness of the TCP coating/underlying alloy interface for the 190-12 sample, as also indicated by ToF-SIMS data, and confirmed by AFM measurements (Fig. 8). Finally, SEM-FEG observations also highlighted a white line at the TCP coating/substrate interface, which was identified by EDS analyses (not shown) as a Cu film [88]. Such a white line was more marked for the 190-12 sample than for the Reference sample, suggesting an increase in the Cu content at least at the TCP coating/substrate interface for the 190—12 sample. This is in agreement with CV results showing a higher θ_{Cu} after degreasing and deoxidation for the 190-12 sample as compared to the Reference sample (Fig. 6) and both ToF-SIMS (Fig. 4) and XPS analyses

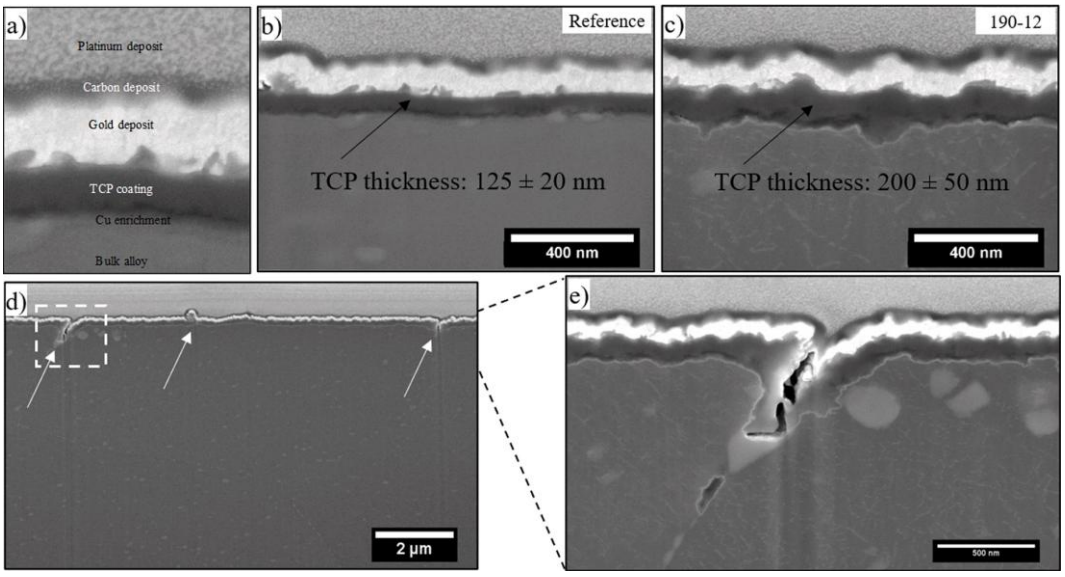

Fig. 10. Cross-sections obtained for TCP coated AA2024 samples. a) Observed area with identification of the different layers, b) Reference sample and c), d), e) 190-12 sample. The horizontal scale cannot be used in the vertical direction due to a tilt of the sample during imaging.

(Fig. 5, Table 1). This particular feature was not observed by ToF-SIMS analysis of the Cu^- signal (Fig. 9), which may be due to the roughness of the TCP coating/substrate interface.

The results show a global increase in thickness of the TCP coating formed on the 190–12 sample. As already discussed in the introduction part, a high Cu amount can be associated with a thicker TCP coating due to the catalytic effect of Cu on the protons reduction, leading to a pH increase and promoting the precipitation of both Cr and Zr oxides and hydroxides [28–31,52,56,88]. It could be assumed that both Cu in the underlying alloy, Cu deposits and Cu-rich intermetallic remnants have this catalytic effect, considering that during immersion in the TCP bath the oxide layer is progressively dissolved by fluoride ions [22]. However, the growth of thicker TCP coating was also associated with a more defective coating due to internal stresses leading to cracking and delamination [28–31,52,56,88]. This was particularly true at the sites where Cu-rich IMCs left Cu deposits or on Cu-rich remnants (Fig. 10d). Furthermore, Fig. 10 (d, e) also shows a defective structure of the TCP coating at the grain boundaries for the 190–12 sample, due to local Cu enrichment associated with the reactivity in the degreasing and deoxidation solution of the Cu-rich intergranular precipitates, in agreement with our previous studies [88].

3.3.2. *Corrosion behaviour of the coated samples*

In order to evaluate the influence of the differences in TCP coating morphology and thickness previously shown between the Reference and 190-12 samples, the corrosion behaviour of the TCP coated samples was studied. Polarisation curves were obtained in a 0.5 M NaCl solution for both samples to evaluate the corrosion protection provided by the TCP coating (Fig. 11). The corrosion potentials E_{corr} of both samples were similar and close to -0.7 V_{SCE}, estimated from preliminary OCP measurements. In the anodic domain, a passivity plateau was observed for the coated Reference sample, whereas a sharp increase in the anodic current density was observed above E_{corr} for the 190–12 sample. The corrosion current densities were determined for both samples. For the Reference sample, the corrosion kinetics was controlled by the oxide layer properties so that the corrosion current density was equal to the passive current density, i.e., about $2\ 10^{-8}$ A cm^{-2}. As the 190—12 sample was susceptible to corrosion at E_{corr}, the corrosion current density for this sample was determined by considering the intersection between the vertical at E_{corr} and the slope of the cathodic branch corresponding to the oxygen reduction reaction. This led to a value of $6\ 10^{-8}$ A cm^{-2}. This result indicates a decrease in the anticorrosion properties of the TCP coating grown on the 190—12 sample with respect to the Reference sample, with a non-passive behaviour of the coated 190—12 sample at E_{corr}, whereas the coated Reference sample remained passive over more than 100 mV above E_{corr}, with a pitting potential value of about – 0.58 V_{SCE}.

The corrosion behaviour of the coated samples was also evaluated by electrochemical impedance spectroscopy for immersion times up to 30 days. For exposure times longer than 1 day, both electrochemical systems, i.e. Reference and 190–12 samples, reached a steady state, and all impedance diagrams showed similar global shape. As an example, the impedance diagram at E_{corr} for the Reference sample, after 7 days of immersion in a 0.5 M NaCl solution, is reported in Bode format in Fig. 12. The high frequency range (> 10^2 Hz) was significantly affected by the ohmic resistance [89–91]. Therefore, the Bode diagrams, i.e. modulus and phase angle diagrams, were corrected for the ohmic resistance (electrolyte resistance R_e 67 Ω cm^2); the ohmic resistance-corrected Bode diagrams are also reported in Fig. 12. Whereas the ohmic resistance obscured the behaviour of the sample in the high frequency range, the corrected phase angle plots clearly showed three time constants. The two time constants corresponding to the low- and medium-frequency ranges corroborate the ToF-SIMS analysis (Fig. 9) that showed a two-layer structure for the TCP coating. The third time constant corresponding to the change in the slope of the modulus vs frequency plot observed in the corrected modulus plot, associated with the abrupt increase of the phase angle for frequencies higher than 1000 Hz, could be attributed to the contribution of the ohmic impedance Z_e [91]. The ohmic impedance Z_e is expressed following Eq. 2 [91]:

$$Z_e = R_{HF} + \frac{R_{LF} - R_{HF}}{(1 + j\omega\tau)^{\alpha^*}} \quad (2)$$

where R_{HF} corresponds to the electrolyte resistance R_e at infinite frequency, R_{LF} is the low-frequency limit of the resistive behaviour, τ and α* the two parameters which correspond to the distribution of time constant [91]. Taking into account those observations, the model used to describe the electrochemical behaviour of the TCP coated samples corresponds to a two-layer coating. On the basis of the literature [92], each layer was considered as a dielectric layer and was characterized by an impedance Z_{ox}, so that the model for the TCP coating corresponds to two impedances in series. Furthermore, at E_{corr}, a parallel resistance R_t had to be considered: it includes the electronic resistance R_{elec} of the TCP coating in series with the charge transfer resistance R_{ct} corresponding to the cathodic oxygen reduction reaction occurring at the electrolyte/TCP coating interface as shown by Eq. 3:

$$R_t = R_{ct} + R_{elec\text{-}1} + R_{elec\text{-}2}, \quad (3)$$

where $R_{elec\text{-}1}$ and $R_{elec\text{-}2}$ refer to the electronic resistance of the external and internal layers of the TCP coating, respectively, even though it was impossible with the calculations to identify each of them. The model includes also the ohmic impedance Z_e so that the impedance of the electrochemical system Z is given by Eq. 4:

$$Z_e = R_{HF} + \frac{R_{LF} - R_{HF}}{(1 + j\omega\tau)^{\alpha^*}} \quad (4)$$

where $Z_{ox\text{-}1}$ and $Z_{ox\text{-}2}$ refer to the imp edance of the external and internal layers of the TCP coating, respectively, even though it was impossible to identify each of them, as previously said for R_{elec} values. $Z_{ox\text{-}1}$ and $Z_{ox\text{-}2}$ were assumed to be well-represented by the power-law model as given by Eq. 5 [92]:

$$Z_{ox} = g(\alpha)\frac{\delta\rho_\delta^{1-\alpha}}{(\rho_0^{-1} + j\omega\varepsilon\varepsilon_0)^\alpha} = \frac{K}{(\rho_0^{-1} + j\omega\varepsilon\varepsilon_0)^\alpha} \quad (5)$$

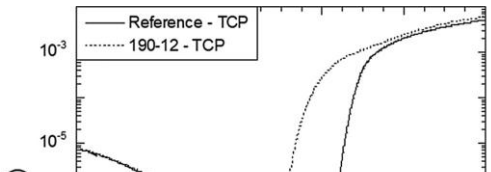

Where

Where $K = g(\alpha)\delta\rho^{1-\alpha.}$ (6)

Fig. 11. Polarisation curves for the TCP coated Reference and 190-12 samples in 0.5 M NaCl. Potential sweep rate = 0.07 mV s^{-1}.

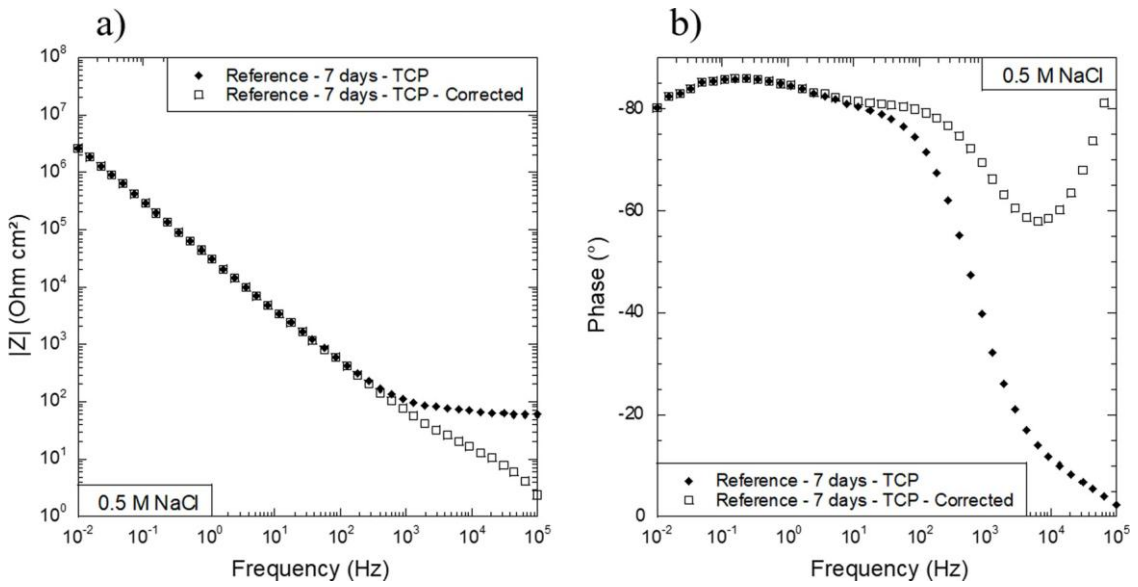

Fig. 12. Impedance diagrams of the Reference TCP coated sample in 0.5 M NaCl after 7 days of immersion at E_{corr}. a) Bode representation: log|Z| vs log(f) and b) Bode representation: phase vs log(f). On each figure, both the experimental and ohmic-resistance-corrected Bode diagrams are reported.

with g a function of α, as defined in [92], α the CPE exponent, ρ_0 and ρ_δ the values of the layer resistivity at each interface of the corresponding layer, respectively, δ the layer thickness, ε the dielectric constant, and ε_0 the permittivity of vacuum.

Finally, as demonstrated by SEM-FEG observations, the total thickness of the TCP coating is 127 and 223 nm for the Reference and 190–12 samples, respectively. Considering a dielectric permittivity of 10 for the two layers [92] and assuming that the two layers have similar thicknesses, the evaluated layer capacitances were significantly lower than the double layer capacitance, so the double layer capacitance could be neglected in the model. A schema of the model is shown in Fig. 13.

Fig. 14 shows the ohmic-resistance-corrected Bode diagram for the Reference and 190–12 samples after 7 and 21 days of exposure to the 0.5 M NaCl solution. Graphical analysis of the impedance modulus showed that the main difference between the Reference and 190–12 samples was the value of the impedance modulus at 10^{-2} Hz, i.e. $|Z|_{0.01\ Hz}$, with $|Z|_{0.01\ Hz}$ values slightly higher for the Reference sample as compared to the 190–12 sample, for both 7 and 21 days of immersion, in agreement with the lower phase for the 190–12 sample at 10^{-2} Hz. To go further in the analysis of the impedance measurements, the experimental impedance values were then fitted by using the model previously described. Fitted data are also reported in Fig. 14. The results show that the differences between the experimental and fitted values are very close for most ranges of frequencies, which indicates that the model is a good representation of the electrochemical systems. The parameters extracted from the model for the EIS data obtained after 7 and 21 days of immersion in 0.5 M NaCl for both the Reference and 190–12 samples are summarised in Table 2. The parameters X for the two layers of the TCP coating are referred to as X_1 and X_2, but, as previously indicated, it was not possible to identify the internal and external layers. The value of the oxide layer impedance at zero frequency can be obtained from Eq. 5 ($Z_{ox}(\omega = 0) = K\rho_0^{\alpha}$): values are reported in Table 2. In each case, $Z_{ox\text{-}1}(\omega = 0) >> Z_{ox\text{-}2}(\omega = 0)$, but comparison between the different samples showed similar values for all $Z_{ox\text{-}1}(\omega 0)$ values and all $Z_{ox\text{-}2}(\omega 0)$ values. Therefore, the difference observed in the low frequency range for the impedance diagram (Fig. 14) was due to the differences in R_t values between the Reference and 190–12 samples as indicated in Table 2. R_t could not be evaluated for the Reference sample, leading us to assume that it was high enough to be neglected in Eq. 4, whereas a value of about 1.07 10^6 Ω cm^2 was calculated for the 190—12 sample. The differences in R_t values could include differences in R_{ct} values between the two samples. This may be linked to an easier cathodic oxygen reduction reaction at the bottom of the TCP defects for the 190–12 sample as compared to the Reference sample, for which the cathodic reaction should take place only on the dense TCP coating. However, considering the polarisation curves shown in Fig. 11, it could be assumed that R_{ct} values are similar for both samples; therefore, the differences in R_t values between the Reference and 190–12 samples should be attributed mainly to the electronic resistance value of the two-layer TCP coating. Then, the results demonstrated that the electronic resistance of the TCP coating was lower for the 190–12 sample than that of the Reference sample, which could be also attributed to the more defective structure of the TCP coating formed on 190—12 sample. However, there was no

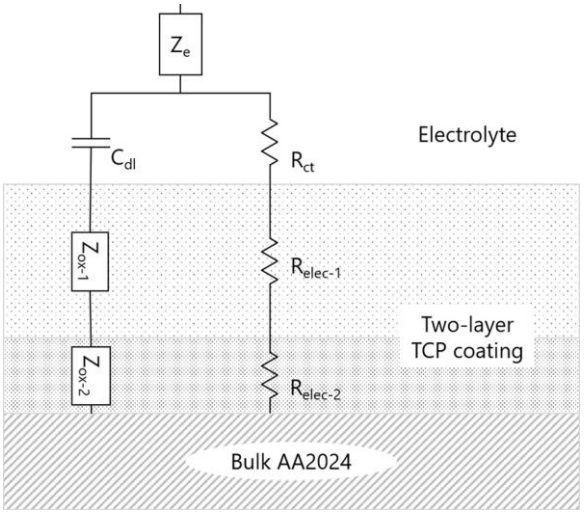

Fig. 13. Model used to analyse the impedance diagrams. In this model, Z_e is the ohmic impedance given by Eq. 2; $Z_{ox\text{-}1}$ and $Z_{ox\text{-}2}$ are the impedance of the external and internal layers of the TCP coating; they are given by Eq. 5. $R_{elec\text{-}1}$ and $R_{elec\text{-}2}$ referred to the electronic resistance of the external and internal layers of the TCP coating.

e

significant variation of the parameters measured for the 190—12 sample

between 7 and 21 days of immersion, which could be seen in Fig. 14 with similar impedance diagrams for both immersion times. This could be assigned to the deposition of some corrosion products leading to an

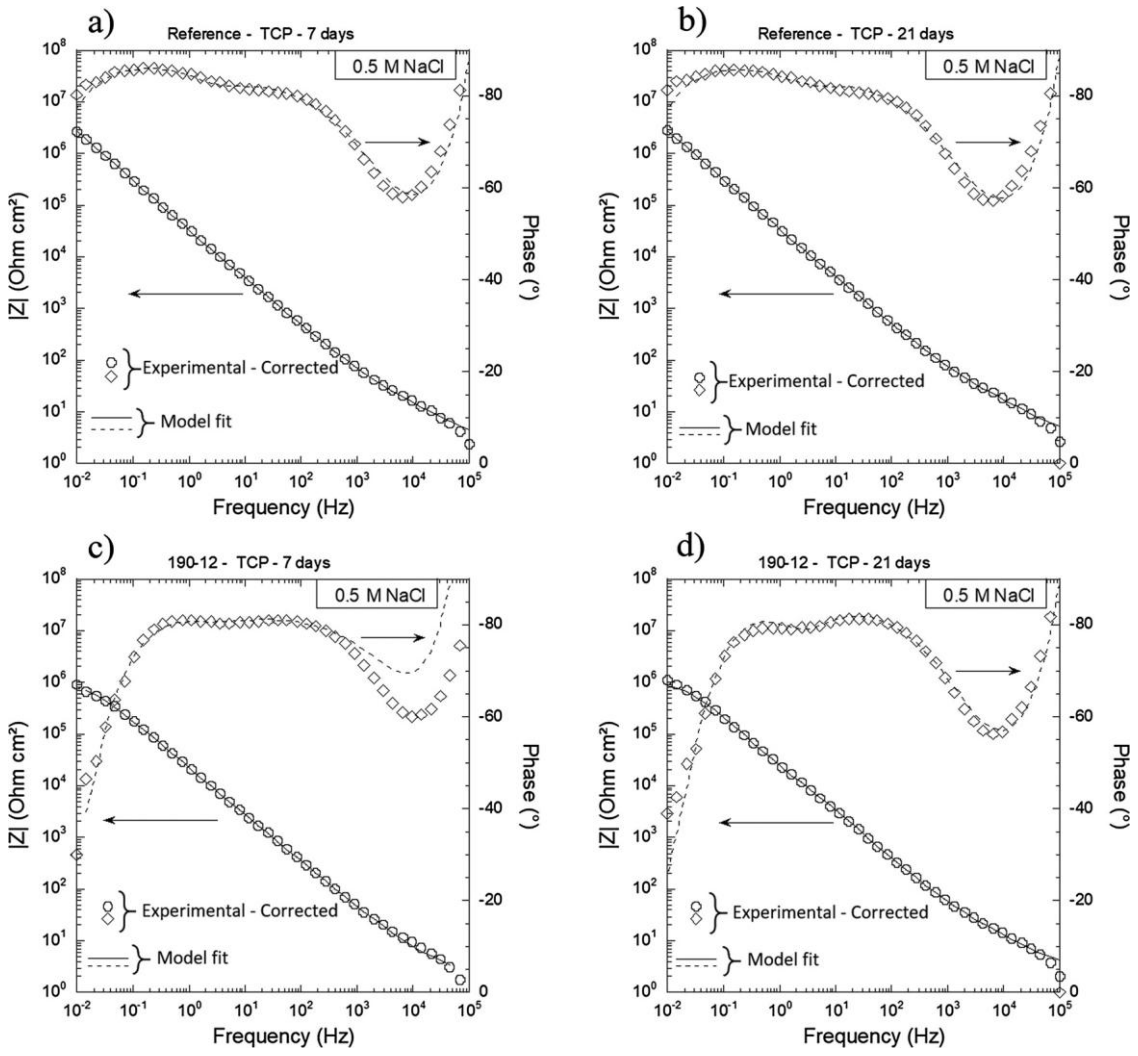

Fig. 14. Experimental and simulated (by using the model shown in Fig. 13) impedance in electrolyte-resistance-corrected Bode representation (log|Z| vs log(f) and phase vs log(f)) for the Reference sample after a) 7 and b) 21 days of immersion in 0.5 M NaCl, and the 190-12 sample after c) 7 and d) 21 days of immersion in 0.5 M NaCl.

Table 2
Parameters extracted from EIS spectra using the model described in Fig. 13.

Parameters	Samples			
	Reference		190–12	
	7 days	21 days	7 days	21 days
α^1	0.96	0.96	0.92	0.95
K^1 ($\Omega^{1-\alpha}$ cm$^{2-\alpha}$)	4.38 10^{-7}	4.87 10^{-7}	8.93 10^{-7}	4.75 10^{-7}
ρ_0^1 (Ω cm)	1.00 10^{14}	1.00 10^{14}	1.00 10^{14}	1.00 10^{14}
$Z_{ox\text{-}1}(\omega = 0)$ (Ω cm^2)	1.21 10^7	1.34 10^7	6.77 10^6	9.48 10^6
α^2	0.75	0.76	0.78	0.92
K^2 ($\Omega^{1-\alpha}$ cm$^{2-\alpha}$)	1.18 10^{-5}	7.36 10^{-6}	1.77 10^{-6}	2.42 10^{-7}
ρ_0^2 (Ω cm)	5.84 10^{10}	5.84 10^{10}	5.85 10^{10}	5.85 10^{10}
$Z_{ox\text{-}2}(\omega = 0)$ (Ω cm^2)	1.40 10^3	1.12 10^3	4.43 10^2	1.95 10^3
R_{HF} (Ω cm^2)	45.2	43.6	9.14	55.8
R_{LF} (Ω cm^2)	187	287	85.4	227
α^*	0.17	0.22	0.02	0.22
τ (μS)	1.53	1.11	0.551	0.47
R_t (Ω cm^2)	∞	∞	1.11 10^6	1.07 10^6
χ	1.03	1.18	1.24	1.50

artificial healing of the TCP coating as the immersion time increased. Moreover, self-healing effects may help to close the coating defects, due to the presence of rare earth elements [93,94]. That said, the impedance results were therefore in agreement with the morphology of the TCP coatings as demonstrated by SEM-FEG, with a very defective structure of the TCP coating formed on the 190 12 sample as compared to the Reference sample.

4. Conclusions

The aim of this work was to investigate the influence of ageing leading to changes in the Cu distribution on the growth and the anti-corrosion properties of a TCP coating on AA2024. The main results are the following:

1 As expected, the ageing treatment at 190 ◦C for 12 h led to the precipitation of Cu in the form of intergranular and hardening nanometer scale precipitates. Combined ToF-SIMS and XPS analyses showed that the ageing treatment led to the thickening of the oxide layer, with an enrichment in Mg, leading to a Mg depletion in the underlying alloy. Both Cu(II) in the oxide layer and metallic Cu in the underlying alloy were observed for the sample aged at 190 ◦C,

whereas only metallic Cu in the underlying alloy was detected for the non-aged sample. Metallic Cu in the underlying alloy was mainly attributed to Cu accumulation at the oxide/metal interface during the growth of the aluminium oxide layer on the Cu-rich solution. Oxidised Cu was linked to a partial oxidation of Cu-rich IMCs, but

also of Cu-rich intergranular precipitates, explaining the differences between the Reference and 190–12 samples, this last alloy containing more numerous and coarser intergranular precipitates.

2 After degreasing and deoxidation, the newly formed oxide films were thicker for both samples than before the pre-treatment, as shown by both ToF-SIMS and XPS analyses. Those two techniques also showed a dissolution of the Mg oxide for both samples during the pre-treatment. Furthermore, during the degreasing and deoxidation, dissolution of the Cu-rich solid solution for both samples followed by the growth on an oxide layer on its surface led to Cu accumulation at the oxide/metal interface. The contribution of Cu-rich intragranular precipitates had to be also considered for the aged samples. This led to an increase in the amount of metallic Cu detected by XPS for both samples. However, metallic Cu could be also assigned to Cu deposits due to the removal of both Cu-rich IMCs and Cu-rich intergranular precipitates. After degreasing and deoxidation, the aged alloy showed more metallic Cu on its surface, which could be mainly attributed to the more numerous and coarser Cu-rich intergranular precipitates as compared to the non-aged sample. These differences between the two samples were also observed by measuring the surface Cu coverage by using cyclic voltammetry measurements leading to higher surface Cu coverage for the aged sample. Oxidised Cu was also observed by ToF-SIMS and XPS for both samples due to partial oxidation of Cu-rich features, i.e. Cu-rich particles remnants and Cu deposits. The enhanced reactivity at the grain boundaries of the aged sample strongly contributed to the increase in the roughness of the aged sample, as revealed by both ToF-SIMS and AFM measurements.

3 The structure and chemical composition of the TCP coating were directly dependent on the Cu enrichment, in agreement with previous literature data. For the aged sample, the Cu coverage increase led to a thicker TCP coating and a rougher TCP coating/substrate interface, as shown by both ToF-SIMS and SEM-FEG. However, thicker TCP coatings also contained more defects, in particular at the grain boundaries. This led to a decrease in their anticorrosion properties corresponding to a decrease in the charge transfer resistance associated to the cathodic oxygen reduction reaction, but also to a decrease in their electronic resistance.

This work clearly shows the influence of Cu on the growth and anticorrosion properties of TCP coating. Attention needs to be paid to both the Cu content and the Cu distribution, i.e. the metallurgical state of the substrate, in order to control the TCP coating chemical composition and structure.

Acknowledgments

This work was performed in the framework of the NEPAL FUI project. CIRIMAT was financially supported by the French Ministry of Economy and industry (BPI-France), the Région Occitanie / Pyrénées - Méditerranée and the European Union (FEDER/ERDF).

Région Ile-de-France is acknowledged for partial funding of the XPS and ToF -SIMS equipment.

The authors are grateful to Bernard Tribollet for fruitful discussions and help for the analysis of impedance measurements.

Appendix A. Supplementary data

Supplementary material related to this article can be found, in the online version.

References

[1] R.J. Hussey, J. Wilson, Light Alloys: Directory and Databook, Springer US, 2013.
[2] D.A. Porter, K.E. Easterling, M. Sherif, Phase Transformations in Metals and Alloys, CRC press, 2009.
[3] M.J. Yin, J.H. Chen, S.B. Wang, Z.R. Liu, L.M. Cha, S.Y. Duan, C.L. Wu, Anisotropic and temperature-dependent growth mechanism of S-phase precipitates in Al–Cu–Mg alloy in relation with GPB zones, Trans. Nonferrous Met. Soc. China 26 (2016) 1–11, https://doi.org/10.1016/S1003-6326(16)64082-7.
[4] R.G. Buchheit, R.P. Grant, P.F. Hlava, B. McKenzie, G.L. Zender, Local dissolution phenomena associated with S phase (Al_2CuMg) particles in aluminum alloy 2024-T3, J. Electrochem. Soc. 144 (1997) 2621–2628. https://iopscience.iop.org/article/10.1149/1.1837874/pdf.
[5] M. Gao, C.R. Feng, R.P. Wei, An analytical electron microscopy study of constituent particles in commercial 7075-T6 and 2024-T3 alloys, Metall. Mater. Trans. A 29 (1998) 1145–1151, https://doi.org/10.1007/s11661-998-0240-9.
[6] R.P. Wei, C.M. Liao, M. Gao, A transmission electron microscopy study of constituent-particle-induced corrosion in 7075-T6 and 2024-T3 aluminum alloys, Metall. Mater. Trans. A 29 (1998) 1153–1160, https://doi.org/10.1007%2Fs11661-998-0241-8.
[7] A. Boag, A.E. Hughes, N.C. Wilson, A. Torpy, C.M. MacRae, A.M. Glenn, T. H. Muster, How complex is the microstructure of AA2024-T3? Corros. Sci. 51 (2009) 1565–1568, https://doi.org/10.1016/j.corsci.2009.05.001.
[8] A.E. Hughes, G.E. Thompson, J.M.C. Mol, N. Birbilis, S.J. Garcia, X. Zhou, High Strength Al-alloys: Microstructure, Corrosion and Principles of Protection, INTECH Open Access Publisher, 2011.
[9] G.S. Chen, M. Gao, R.P. Wei, Microconstituent-induced pitting corrosion in aluminum alloy 2024-T3, Corrosion 52 (1996) 8–15, https://doi.org/10.5006/1.3292099.
[10] V. Guillaumin, G. Mankowski, Localized corrosion of 2024 T351 aluminium alloy in chloride media, Corros. Sci. 41 (1998) 421–438, https://doi.org/10.1016/ S0010-938X(98)00116-4.
[11] L. Lacroix, C. Blanc, N. Pébère, G.E. Thompson, B. Tribollet, V. Vivier, Simulating the galvanic coupling between S-Al_2CuMg phase particles and the matrix of 2024 aerospace aluminium alloy, Corros. Sci. 64 (2012) 213–221, https://doi.org/10.1016/j.corsci.2012.07.020.
[12] A. Boag, A.E. Hughes, A.M. Glenn, T.H. Muster, D. McCulloch, Corrosion of AA2024-T3 part I: localised corrosion of isolated IM particles, Corros. Sci. 53 (2011) 17–26, https://doi.org/10.1016/j.corsci.2010.09.009.
[13] N. Birbilis, R.G. Buchheit, Electrochemical characteristics of intermetallic phases in aluminum alloys an experimental survey and discussion, J. Electrochem. Soc. 152 (2005) B140–B151, https://doi.org/10.1149/1.1869984.
[14] R. Grilli, M.A. Baker, J.E. Castle, B. Dunn, J.F. Watts, Localized corrosion of a 2219 aluminium alloy exposed to a 3.5% NaCl solution, Corros. Sci. 52 (2010) 2855–2866, https://doi.org/10.1016/j.corsci.2010.04.035.
[15] M. Kendig, S. Jeanjaquet, R. Addison, J. Waldrop, Role of hexavalent chromium in the inhibition of corrosion of aluminum alloys, Surf. Coat. Technol. 140 (2001) 58–66, https://doi.org/10.1016/S0257-8972(01)01099-4.
[16] L. Xia, R.L. McCreery, Chemistry of a chromate conversion coating on aluminum alloy AA2024-T3 probed by vibrational spectroscopy, J. Electrochem. Soc. 145 (1998) 3083–3089, https://doi.org/10.1149/1.1838768.
[17] J. Zhao, G. Frankel, R.L. McCreery, Corrosion protection of untreated AA-2024-T3 in chloride solution by a chromate conversion coating monitored with raman spectroscopy, J. Electrochem. Soc. 145 (1998) 2258–2264. https://iopscience.iop.org/article/10.1149/1.1838630/pdf.

[18] E. Eichinger, J. Osborne, T. Van Cleave, Hexavalent chromium elimination: an aerospace industry progress report, Met. Finish. 95 (1997) 36–41, https://doi.org/10.1016/S0026-0576(97)86771-2.
[19] J. Zhao, L. Xia, A. Sehgal, D. Lu, R.L. McCreery, G.S. Frankel, Effects of chromate and chromate conversion coatings on corrosion of aluminum alloy 2024-T3, Surf. Coat. Technol. 140 (2001) 51–57, https://doi.org/10.1016/S0257-8972(01)01003-9.
[20] S. Merenyi, REACH: Regulation (EC) No 1907/2006: Consolidated Version (June 2012) With an Introduction and Future Prospects Regarding the Area of Chemicals Legislation, GRIN Verlag, 2012.
[21] C. Matzdorf, M. Kane, J. Green, Corrosion resistant coatings for aluminum and aluminum alloys. United States, NAVY CHIEF OF NAVAL RESEARCH THE, Secretary of US Secretary of Navy, 2002.
[22] X. Verdalet-Guardiola, B. Fori, J.P. Bonino, S. Duluard, C. Blanc, Nucleation and growth mechanisms of trivalent chromium conversion coatings on 2024-T3 aluminium alloy, Corros. Sci. 155 (2019) 109–120, https://doi.org/10.1016/j.corsci.2019.04.035.
[23] M. Ely, J. Światowska, A. Seyeux, S. Zanna, P. Marcus, Role of post-treatment in improved corrosion behavior of trivalent chromium protection (TCP) coating deposited on aluminum alloy 2024-T3, J. Electrochem. Soc. 164 (2017) C276–C284, https://doi.org/10.1149/2.0431706jes.
[24] Y. Guo, G.S. Frankel, Characterization of trivalent chromium process coating on AA2024-T3, Surf. Coat. Technol. 206 (2012) 3895–3902, https://doi.org/10.1016/j.surfcoat.2012.03.046.
[25] X. Dong, P. Wang, S. Argekar, D.W. Schaefer, Structure and composition of trivalent chromium process (TCP) films on Al alloy, Langmuir 26 (2010) 10833–10841, https://doi.org/10.1021/la100699u.
[26] S. Dardona, M. Jaworowski, In situ spectroscopic ellipsometry studies of trivalent chromium coating on aluminum, Appl. Phys. Lett. 97 (2010) 181908, https://doi.org/10.1063/1.3511472.
[27] L. Li, A.L. Desouza, G.M. Swain, In situ pH measurement during the formation of conversion coatings on an aluminum alloy (AA2024), Analyst 138 (2013) 4398–4402, https://doi.org/10.1039/C3AN00663H.
[28] J. Qi, T. Hashimoto, J. Walton, X. Zhou, P. Skeldon, G.E. Thompson, Formation of a trivalent chromium conversion coating on AA2024-T351 alloy, J. Electrochem. Soc. 163 (2016) C25–C35, https://doi.org/10.1149/2.0771602jes.
[29] C.A. Munson, G.M. Swain, Structure and chemical composition of different variants of a commercial trivalent chromium process (TCP) coating on aluminum alloy 7075-T6, Surf. Coat. Technol. 315 (2017) 150–162, https://doi.org/10.1016/j.surfcoat.2017.02.018.
[30] L. Li, K.P. Doran, G.M. Swain, Electrochemical characterization of trivalent chromium process (TCP) coatings on aluminum alloys 6061 and 7075, J. Electrochem. Soc. 160 (2013) C396–C401, https://doi.org/10.1149/2.117308jes.
[31] Q. Meng, G.S. Frankel, Effect of copper content on chromate conversion coating protection of 7xxx-T6 aluminum alloys, Corrosion 60 (2004) 897–905, https://doi.org/10.5006/1.3287823.
[32] M.A. Jakab, D.A. Little, J.R. Scully, Experimental and modeling studies of the oxygen reduction reaction on AA2024-T3, J. Electrochem. Soc. 152 (2005) B311–B320, https://doi.org/10.1149/1.1949047.
[33] D.A. Little, M.A. Jakab, J.R. Scully, Effect of surface pretreatment on the underpaint corrosion of AA2024-T3 at various temperatures, Corrosion 62 (2006) 300–315, https://doi.org/10.5006/1.3280663.
[34] A.J. Davenport, B. Liu, Copper accumulation during cleaning of Al–Cu alloys, in: R. G. Buchheit, B.A. Shaw, J.P. Moran (Eds.), Corrosion and Corrosion Prevention of Low Density Metals and Alloys, The Electrochemical Society Proceedings Series, Pennington, NJ, 2000. PV 2000-23, p. 41.
[35] Z. Huda, N.I. Taib, T. Zaharinie, Characterization of 2024-T3: an aerospace aluminum alloy, Mater. Chem. Phys. 113 (2009) 515–517, https://doi.org/10.1016/j.matchemphys.2008.09.050.
[36] AA 2024-T3/T351 Alloy Sheet: the Influence of Grain Size on Crack Propagation and Fracture Toughness Behaviour, AluReport, 2020, pp. 12–13.
[37] P.J. Hurley, F.J. Humphreys, A study of recrystallization in single-phase aluminium using in-situ annealing in the scanning electron microscope, J. Microsc. 213 (2004) 225–234, https://doi.org/10.1111/j.0022-2720.2004.01300.x.
[38] A.E. Hughes, R. Parvizi, M. Forsyth, Microstructure and corrosion of AA2024, Corros. Rev. 33 (2015) 1–30, https://doi.org/10.1515/corrrev-2014-0039.
[39] P. Campestrini, E.P.M. van Westing, H.W. van Rooijen, J.H.W. de Wit, Relation between microstructural aspects of AA2024 and its corrosion behaviour investigated using AFM scanning potential technique, Corros. Sci. 42 (2000) 1853–1861, https://doi.org/10.1016/S0010-938X(00)00002-0.
[40] N.D. Alexopoulos, Z. Velonaki, C.I. Stergiou, S.K. Kourkoulis, The effect of artificial ageing heat treatments on the corrosion-induced hydrogen embrittlement of 2024 (Al–Cu) aluminium alloy, Corros. Sci. 102 (2016) 413–424, https://doi.org/10.1016/j.corsci.2015.10.034.
[41] C.K.S. Moy, M. Weiss, J. Xia, G. Sha, S.P. Ringer, G. Ranzi, Influence of heat treatment on the microstructure, texture and formability of 2024 aluminium alloy, Mater. Sci. Eng. A 552 (2012) 48–60, https://doi.org/10.1016/j.msea.2012.04.113.
[42] S.P. Ringer, K. Hono, Microstructural evolution and age hardening in aluminium alloys: atom probe field-ion microscopy and transmission electron microscopy studies, Mater. Charact. 44 (2000) 101–131, https://doi.org/10.1016/S1044-5803(99)00051-0.
[43] T.J. Bastow, A.J. Hill, Guinier-Preston and Guinier-Preston-Bagaryatsky zone reversion in Al-Cu-Mg alloys studied by NMR. Materials Science Forum, Trans Tech Publ, 2006, pp. 1385–1390, https://doi.org/10.4028/www.scientific.net/MSF.519-521.1385.
[44] Y.A. Bagaryatsky, Structural Changes on Aging Al–Cu–Mg Alloys, Dokl Akad SSSR, 1952, pp. 397–559.
[45] S.C. Wang, M.J. Starink, Precipitates and intermetallic phases in precipitation hardening Al–Cu–Mg–(Li) based alloys, Int. Mater. Rev. 50 (2005) 193–215, https://doi.org/10.1179/174328005X14357.
[46] S.C. Wang, M.J. Starink, N. Gao, Precipitation hardening in Al–Cu–Mg alloys revisited, Scr. Mater. 54 (2006) 287–291, https://doi.org/10.1016/j.scriptamat.2005.09.010.
[47] S.C. Wang, M.J. Starink, Two types of S phase precipitates in Al–Cu–Mg alloys, Acta Mater. 55 (2007) 933–941, https://doi.org/10.1016/j.actamat.2006.09.015.
[48] H. Perlitz, A. Westgren, Arkiv kemi mineral, Geol (1943).
[49] E.A. Starke, J.T. Staley, Application of modern aluminum alloys to aircraft, Prog. Aerosp. Sci. 32 (1996) 131–172, https://doi.org/10.1016/0376-0421(95)00004-6.
[50] G. Sha, R.K.W. Marceau, X. Gao, B.C. Muddle, S.P. Ringer, Nanostructure of aluminium alloy 2024: segregation, clustering and precipitation processes, Acta Mater. 59 (2011) 1659–1670, https://doi.org/10.1016/j.actamat.2010.11.033.
[51] Y.C. Lin, Y.C. Xia, Y.Q. Jiang, H.M. Zhou, L.T. Li, Precipitation hardening of 2024-T3 aluminum alloy during creep aging, Mater. Sci. Eng. A 565 (2013) 420–429, https://doi.org/10.1016/j.msea.2012.12.058.
[52] R. Saillard, B. Viguier, G. Odemer, A. Pugliara, B. Fori, C. Blanc, Influence of the microstructure on the corrosion behaviour of 2024 aluminium alloy coated with a trivalent chromium conversion layer, Corros. Sci. 142 (2018) 119–132, https://doi.org/10.1016/j.corsci.2018.07.007.
[53] B. Heying, R.D. Hoffmann, R. Pöttgen, Structure Refinement of the S-Phase Precipitate $MgCuAl_2$, Zeitschrift für Naturforschung B, 2005, p. 491, https://doi.org/10.1002/chin.200533004.
[54] J. Zhang, Y.N. Huang, C. Mao, P. Peng, Structural, elastic and electronic properties of θ (Al_2Cu) and S (Al_2CuMg) strengthening precipitates in Al–Cu–Mg series alloys: first-principles calculations, Solid State Commun. 152 (2012) 2100–2104, https://doi.org/10.1016/j.ssc.2012.09.003.
[55] A.I. Stoica, J. Światowska, A. Romaine, F. Di Franco, J. Qi, D. Mercier, A. Seyeux, S. Zanna, P. Marcus, Influence of post-treatment time of trivalent chromium protection coating on aluminium alloy 2024-T3 on improved corrosion resistance, Surf. Coat. Technol. 369 (2019) 186–197, https://doi.org/10.1016/j.surfcoat.2019.04.051.
[56] R. Viroulaud, J. Światowska, A. Seyeux, S. Zanna, J. Tardelli, P. Marcus, Influence of surface pretreatments on the quality of trivalent chromium process coatings on aluminum alloy, Appl. Surf. Sci. 423 (2017) 927–938, https://doi.org/10.1016/J.APSUSC.2017.06.246.
[57] P. Cornette, S. Zanna, A. Seyeux, D. Costa, P. Marcus, The native oxide film on a model aluminium-copper alloy studied by XPS and ToF-SIMS, Corros. Sci. (2020) 108837, https://doi.org/10.1016/j.corsci.2020.108837.
[58] C. Lea, C. Molinari, Magnesium diffusion, surface segregation and oxidation in Al-Mg alloys, J. Mater. Sci. 19 (1984) 2336–2352, https://doi.org/10.1007/BF01058110.
[59] R.G. Song, W. Dietzel, B.J. Zhang, W.J. Liu, M.K. Tseng, A. Atrens, Stress corrosion cracking and hydrogen embrittlement of an Al–Zn–Mg–Cu alloy, Acta Mater. 52 (2004) 4727–4743, https://doi.org/10.1016/j.actamat.2004.06.023.
[60] R.G. Song, M.K. Tseng, B.J. Zhang, J. Liu, Z.H. Jin, K.S. Shin, Grain boundary segregation and hydrogen-induced fracture in 7050 aluminium alloy, Acta Mater. 44 (1996) 3241–3248, https://doi.org/10.1016/j.actamat.2004.06.023.
[61] S.O. Saied, J.L. Sullivan, A study of thermally induced segregation of magnesium in aluminium-magnesium alloys by means of AES, J. Phys. Condens. Matter 5 (1993) A165. https://iopscience.iop.org/article/10.1088/0953-8984/5/33A/043/pdf.
[62] K. Domen, T.J. Chuang, Laser induced photodissociation and desorption. I. CH_2I_2 adsorbed on Al_2O_3, J. Chem. Phys. 90 (1989) 3318–3331, https://doi.org/10.1063/1.455886.
[63] S.J. Splinter, N.S. McIntyre, W.N. Lennard, K. Griffiths, G. Palumbo, An AES and XPS study of the initial oxidation of polycrystalline magnesium with water vapour at room temperature, Surf. Sci. 292 (1993) 130–144, https://doi.org/10.1016/0039-6028(93)90396-2.
[64] N.S. McIntyre, C. Chen, Role of impurities on Mg surfaces under ambient exposure conditions, Corros. Sci. 40 (1998) 1697–1709, https://doi.org/10.1016/S0010-938X(98)00072-9.
[65] G. Deroubaix, P. Marcus, X-ray photoelectron spectroscopy analysis of copper and zinc oxides and sulphides, Surf. Interface Anal. 18 (1992) 39–46, https://doi.org/10.1002/sia.740180107.
[66] K.-A. Son, N. Missert, J.C. Barbour, J.J. Hren, R.G. Copeland, K.G. Minor, Growth and oxidation of thin film Al_2Cu, J. Electrochem. Soc. 148 (2001) B260, https://doi.org/10.1149/1.1376635.
[67] Y. Liu, P. Bailey, T.C.Q. Noakes, G.E. Thompson, P. Skeldon, M.R. Alexander, Chemical environment of copper at the surface of a $CuAl_2$ model alloy: XPS, MEIS and TEM analyses, Surf. Interface Anal. 36 (2004) 339–346, https://doi.org/10.1002/sia.1743.
[68] A. Seyeux, G.S. Frankel, N. Missert, K.A. Unocic, L.H. Klein, A. Galtayries, P. Marcus, ToF-SIMS imaging study of the early stages of corrosion in Al-Cu thin films, J. Electrochem. Soc. 158 (2011) C165–C171, https://doi.org/10.1149/1.3568944.
[69] M. Li, F. Wiame, A. Seyeux, P. Marcus, J. Światowska, Effect of thermal oxidation on surface chemistry and elemental segregation of Al-Cu-Li alloy, Appl. Surf. Sci. 534 (2020) 147633, https://doi.org/10.1016/j.apsusc.2020.147633.
[70] Y. Liu, F. Colin, P. Skeldon, G. Thompson, X. Zhou, H. Habazaki, K. Shimizu, Enrichment factors for copper in aluminium alloys following chemical and

electrochemical surface treatments, Corros. Sci. 45 (2003) 1539–1544, https://doi.org/10.1016/S0010-938X(02)00249-4.
[71] X. Zhou, G. Thompson, H. Habazaki, K. Shimizu, P. Skeldon, G. Wood, Copper enrichment in Al-Cu alloys due to electropolishing and anodic oxidation, Thin Solid Films 293 (1997) 327–332, https://doi.org/10.1016/S0040-6090(96)09117-1.
[72] H. Habazaki, K. Shimizu, M.A. Paez, P. Skeldon, G. Thompson, G.C. Wood, X. Xhou, Oxidation of copper and mobility of copper ions during anodizing of an Al-1.5 wt.% Cu alloy, Surf. Interface Anal. 23 (1995) 892–898, https://doi.org/10.1002/sia.740231307.
[73] T. Hashimoto, X. Zhou, P. Skeldon, G. Thompson, Structure of the copper-enriched layer introduced by anodic oxidation of copper-containing aluminium alloy, Electrochim. Acta 179 (2015) 394–401, https://doi.org/10.1016/j.electacta.2015.01.133.
[74] X. Zhou, G. Thompson, J. Robinson, P. Skeldon, X-ray absorption spectroscopy study of the incorporated copper species in anodic alumina films formed on a Al-2 wt% Cu alloy, J. Electrochem. Soc. 152 (2005) B393–B396, https://doi.org/10.1149/1.2007087.
[75] C. Blanc, A. Freulon, M.C. Lafont, Y. Kihn, G. Mankowski, Modelling the corrosion behaviour of Al_2CuMg coarse particles in copper-rich aluminium alloys, Corros. Sci. 48 (2006) 3838–3851, https://doi.org/10.1016/j.corsci.2006.01.012.
[76] Y. Liu, P. Skeldon, G.E. Thompson, H. Habazaki, Anodic film growth on an Al–21at. % Mg alloy, Corros. Sci. 44 (2002) 1133–1142, https://doi.org/10.1016/S0010-938X(01)00115-9.
[77] A.E. Hughes, T.G. Harvey, T. Nikpour, T.H. Muster, S.G. Hardin, Non-chromate deoxidation of AA2024-T3 using Fe (III)–HF–HNO_3, Surf. Interface Anal. 36 (2004) 15–23, https://doi.org/10.1002/sia.1998.
[78] C.E. Caicedo-Martinez, E. Koroleva, P. Skeldon, G.E. Thompson, G. Hoellrigl, P. Bailey, T.C.Q. Noakes, H. Habazaki, K. Shimizu, Behavior of impurity and minor alloying elements during surface treatments of aluminum, J. Electrochem. Soc. 149 (2002) B139–B145, https://doi.org/10.1149/1.1457982.
[79] T.G. Harvey, A.E. Hughes, S.G. Hardin, T. Nikpour, S.K. Toh, A. Boag, D. McCulloch, M. Horne, Non-chromate deoxidation of AA2024-T3: Sodium bromate–nitric acid (20–60° C), Appl. Surf. Sci. 254 (2008) 3562–3575, https://doi.org/10.1016/j.apsusc.2007.11.061.
[80] J. Vander Kloet, A.W. Hassel, M. Stratmann, Effect of pretreatment on the intermetallics in aluminum alloy 2024-T3, Zeitschrift für Physikalische Chemie 219 (2005) 1505–1518, https://doi.org/10.1524/zpch.2005.219.11.1505.
[81] C.E. Caicedo-Martinez, E.V. Koroleva, G.E. Thompson, P. Skeldon, K. Shimizu, H. Habazaki, G. Hoellrigl, Surface nanotextures on aluminium, Surf. Interface Anal. 34 (2002) 405–408, https://doi.org/10.1002/sia.1327.
[82] K.D. Ralston, N. Birbilis, M.K. Cavanaugh, M. Weyland, B.C. Muddle, R.K. W. Marceau, Role of nanostructure in pitting of Al–Cu–Mg alloys, Electrochim. Acta 55 (2010) 7834–7842, https://doi.org/10.1016/j.electacta.2010.02.001.
[83] J. Cerezo, I. Vandendael, R. Posner, K. Lill, J.H.W. De Wit, J.M.C. Mol, H. Terryn, Initiation and growth of modified Zr-based conversion coatings on multi-metal surfaces, Surf. Coat. Technol. 236 (2013) 284–289, https://doi.org/10.1016/j.surfcoat.2013.09.059.
[84] F. Andreatta, A. Turco, I. De Graeve, H. Terryn, J.H.W. De Wit, L. Fedrizzi, SKPFM and SEM study of the deposition mechanism of Zr/Ti based pre-treatment on AA6016 aluminum alloy, Surf. Coat. Technol. 201 (2007) 7668–7685, https://doi.org/10.1016/j.surfcoat.2007.02.039.
[85] J.T. Qi, T. Hashimoto, J.R. Walton, X. Zhou, P. Skeldon, G.E. Thompson, Trivalent chromium conversion coating formation on aluminium, Surf. Coat. Technol. 280 (2015) 317–329, https://doi.org/10.1016/j.surfcoat.2015.09.024.
[86] X. Verdalet-Guardiola, J.P. Bonino, S. Duluard, B. Fori, C. Blanc, Influence of the alloy microstructure and surface state on the protective properties of trivalent chromium coatings grown on a 2024 aluminium alloy, Surf. Coat. Technol. 344 (2018) 276–287, https://doi.org/10.1016/j.surfcoat.2018.03.046.
[87] L. Li, G.P. Swain, A. Howell, D. Woodbury, G.M. Swain, The formation, structure, electrochemical properties and stability of trivalent chrome process (TCP) coatings on AA2024, J. Electrochem. Soc. 158 (2011) C274–C283, https://doi.org/10.1149/1.3607980.
[88] X. Verdalet-Guardiola, R. Saillard, B. Fori, S. Duluard, C. Blanc, Comparative analysis of the anticorrosive properties of trivalent chromium conversion coatings formed on 2024-T3 and 2024-T351 aluminium alloys, Corros. Sci. (2020) 108508, https://doi.org/10.1016/j.corsci.2020.108508.
[89] M.-E. Orazem, N. Pébère, B. Tribollet, Enhanced graphical representation of electrochemical impedance data, J. Electrochem. Soc. 153 (2006) B129–B136, https://doi.org/10.1149/1.2168377.
[90] T.T.M. Tran, B. Tribollet, E.M.M. Sutter, New insights into the cathodic dissolution of aluminium using electrochemical methods, Electrochim. Acta 216 (2016) 58–67, https://doi.org/10.1016/j.electacta.2016.09.011.
[91] O. Gharbi, A. Dizon, M.E. Orazem, M.T.T. Tran, B. Tribollet, V. Vivier, From frequency dispersion to ohmic impedance: a new insight on the high-frequency impedance analysis of electrochemical systems, Electrochim. Acta 320 (2019) 134609, https://doi.org/10.1016/j.electacta.2019.134609.
[92] B. Tribollet, V. Vivier, M.E. Orazem, EIS technique in passivity studies: determination of the dielectric properties of passive films. Encyclopedia of Interfacial Chemistry: Surface Science and Electrochemistry, Elsevier, 2017, pp. 1–14.
[93] K.A. Yasakau, M.L. Zheludkevich, S.V. Lamaka, M.G.S. Ferreira, Mechanism of corrosion inhibition of AA2024 by rare-earth compounds, J. Phys. Chem. B 110 (2006) 5515–5528, https://doi.org/10.1021/jp0560664.
[94] M. Bethencourt, F.J. Botana, J.J. Calvino, M. Marcos, M.A. Rodriguez-Chacon, Lanthanide compounds as environmentally-friendly corrosion inhibitors of aluminium alloys: a review, Corros. Sci. 40 (1998) 1803–1819, https://doi.org/10.1016/S0010-938X(98)00077-8.